A Numerical Model of Stress Driven Grain Boundary Diffusion

J. A. Sethian * and Jon Wilkening **

Department of Mathematics and Lawrence Berkeley National Laboratory,
University of California, Berkeley, CA 94721.

Abstract

The stress driven grain boundary diffusion problem is a continuum model of mass transport phenomena in microelectronic circuits due to high current densities (electromigration) and gradients in normal stress along grain boundaries. The model involves coupling many different equations and phenomena, and difficulties such as non-locality, stiffness, complex geometry, and singularities in the stress tensor near corners and junctions make the problem difficult to analyze rigorously and simulate numerically. We present a new numerical approach to this problem using techniques from semigroup theory to represent the solution. The generator of this semigroup is the composition of a type of Dirichlet to Neumann map on the grain boundary network with the Laplace operator on the network. To compute the former, we solve the equations of linear elasticity several times, once for each basis function on the grain boundary. We resolve singularities in the stress field near corners and junctions by adjoining special singular basis functions to both finite element spaces (2d for elasticity, 1d for grain boundary functions). We develop data structures to handle jump discontinuities in displacement across grain boundaries, singularities in the stress field, complicated boundary conditions at junctions and interfaces, and the lack of a natural ordering for the nodes on a branching grain boundary network. The method is used to study grain boundary diffusion for several geometries.

Key words: grain boundary, electromigration, elasticity, corner singularity, finite element method
MSC: 65J10, 74F99, 47D03

---

* This author was supported in part by the Applied Mathematical Science subprogram of the Office of Energy Research, U.S. Department of Energy, and the Division of Mathematical Sciences of the National Science Foundation.

** Corresponding author. Current address: Courant Institute of Mathematical Sciences, New York, NY 10012. This author was supported in part by a Department of Energy Computational Science Graduate Student Fellowship and by the National Science Foundation through grant DMS-0101439.

Email addresses: `sethian@math.berkeley.edu` (J. A. Sethian), `wilken@cims.nyu.edu` (Jon Wilkening).

Preprint submitted to Journal of Computational Physics *March 20, 2003*

1 Introduction

Mass transport phenomena play a significant role in the failure of microelectronic circuits. Current densities as high as $10^6 \mathrm{A/cm}^2$ are typical in the interconnect lines of these circuits. Electromigration is a diffusion process in which high current densities act as a driving force to transport ions in a metallic lattice in the direction of electron flow by transferring momentum through scattering. Grain boundaries, void surfaces, and passivation interfaces are fast diffusion paths along which the diffusion constant is typically 7-8 orders of magnitude higher than in the grains; therefore, most of the mass transport occurs at these locations. The inhomogeneous redistribution of atoms leads to the development of stresses in the line. Stress gradients along grain boundaries and surface tension at void surfaces both contribute to the flux of atoms, usually suppressing electromigration and increasing the lifetime of the line.

Many theoretical models have been proposed to explain the role of various combinations of electromigration, stress gradients, diffusion, temperature, anisotropy, surface tension, and hillock formation on the mass transport of atoms in the bulk grains, along void surfaces, along grain boundaries, and at passivation interfaces. The survey article by Ho and Kwok [1] and the book by Tu, Mayer and Feldman [2] describe the physics underlying many of these models from the engineering perspective, with current and historical references. See also Mullins [3], which provides a nice overview of mass transport along surfaces and interfaces.

Several numerical methods have recently been developed to study grain growth and void evolution. Schimschak and Krug [4] use a boundary element method to follow the evolution of a void in an infinite domain with a boundary condition on current at infinity. They investigate the stability of the void shape and speed of propagation as a function of void size. Li et. al. [5] and Averbuch et. al. [6] employ level set methods to track void evolution due to electromigration and surface diffusion for a finite geometry. Power dissipation models of curvature driven grain boundary motion have led to several deterministic and stochastic methods for simulating the evolution of microstructure; see e.g. Cocks and Gill [7] and Moldovan et. al. [8]. Haslam et. al. [9] use molecular dynamics simulations to study grain growth and grain rotation. Demirel et. al. [10] have shown that anisotropic effects of grain boundary mobility on misorientation must be taken into account to obtain predictive annealing simulations. None of these models include the effect of stress.

Kirchheim [11] and Korhonen et. al. [12] study the role of stress in the electromigration process. Kirchheim develops a model of stress generation based on vacancy formation in the bulk grains, while Korhonen et. al. make a statistical argument about the distribution of grain boundaries to study the influence of stress on grain boundary diffusion. Both papers use a scalar "effective" stress field rather than actually solving the elasticity equations for the stress tensor. This yields qualitative insight, but ignores the fact that for any particular sample, the geometry of the grain boundaries will greatly affect the stress field, and can lead to large stress concentrations near corners and junctions which can significantly influence the diffusion process.

Bower, Craft, Fridline and collaborators use an advancing front algorithm to generate a sequence of adaptive, evolving finite element meshes to solve the two dimensional linear elasticity equations repeatedly as the geometry changes. They have studied grain growth, void evolution, hillock formation, and grain boundary sliding for possibly anisotropic materials responding to stress, surface tension, thermal expansion, and electromigration; see e.g. [13,14]. They use interesting semi-implicit techniques to overcome timestep limitations due to the stiffness of the equations, and Lagrange multipliers to determine the normal stress along grain boundaries.

This paper is the numerical counterpart to [15], which provides a mathematical framework in which a modest subset of the physical phenomena mentioned above can be studied rigorously. Notably absent from our model are void migration and curvature driven grain boundary motion. These phenomena have been studied many times elsewhere, neglecting stress. Our goal is to present a careful study of the role of stress in the diffusion process, which poses many challenges by itself. The equations are stiff and non-local: growth rates depend on taking two derivatives of normal stress along grain boundaries, while the normal stress is obtained from the net grain growth by solving the equations of linear elasticity with non-standard interface boundary conditions. The geometry of the problem involves the complicated branching structure of a grain boundary network which does not have a natural ordering or orientation of its segments. Boundary conditions specify the gradient of the normal stress at junctions where the stress field is singular. Both displacement and flux boundary conditions are specified at junctions where grain boundaries meet the outer walls; analogy with the heat equation leads to the erroneous conclusion that they have been over-specified, while brute force numerical methods are inconclusive at these junctions due to singularities in the stress field.

Our model is identical to that used in [13], except that they model each side of the grain boundary as a moving interface, whereas we have formulated the problem as an evolution of the jump in displacement $g = (\mathbf{u}^+ - \mathbf{u}^-) \cdot \mathbf{n}$ across the grain boundary Γ, treating g as a *function* defined on the fixed set Γ. Here $\mathbf{n}$ is the unit normal to Γ and $\mathbf{u}^\pm$ are the limiting values of displacement on either side of the grain boundary, labeled so that $\mathbf{n}$ points into the $(+)$ grain. This viewpoint allows us to recast the problem as an ordinary differential equation on a Hilbert space and apply techniques from semigroup theory to prove that the problem is well-posed. The difficulties due to non-locality, the existence of singularities, and the complicated nature of the boundary conditions are all absorbed into two unbounded operators L and S, which turn out to possess many nice properties such as self-adjointness, discrete spectra, and positivity (or negativity); see [15]. Our numerical method is also based on this reformulation as an ODE on a Hilbert space. We compute the decay rates and eigenmodes of the dynamics using special techniques to accurately resolve stress singularities. These provide physical insight about the evolution process, elucidate the theory developed in [15], and may be used to quickly compute the state of the system at any time without time-stepping. The overhead of computing the generator of the semigroup is computationally equivalent to taking a few hundred timesteps.

In Sec. 2, we exhibit the equations in dimensionless form and briefly describe the physical considerations which lead to these equations. In Sec. 3, we summarize those aspects of the theory of stress driven grain boundary diffusion developed in [15,16] which are necessary for developing our numerical method. In particular, we define the operators L and S mentioned above, show how to represent the semigroup governing the evolution of normal stress in terms of the eigenvalues and eigenfunctions of a compact operator, and explain why it is possible to impose boundary conditions on the derivative of normal stress at junctions where the stress tensor is singular.

In Sec. 4, we describe our numerical algorithm, which involves computing a type of Neumann to Dirichlet map on the grain boundary, explicitly capturing singular asymptotic behavior in the stress field, solving the Poisson problem on a network geometry with junctions, and symmetrizing an almost symmetric matrix. We maintain two levels of finite element structures which can readily communicate with each other: the first is a large finite element space on which the two dimensional Laplace and Lamé equations are solved, and the second is a small finite element space on which the normal stress $\eta = \mathbf{n}\cdot\sigma\mathbf{n}$ and displacement jump $g = (\mathbf{u}^+ - \mathbf{u}^-)\cdot\mathbf{n}$ evolve as functions defined on Γ. Data structures are developed which can cope with the complications of jump discontinuities across grain boundaries, singularities in the stress field, non-trivial boundary conditions at junctions and interfaces, and the lack of a natural ordering for the nodes on a branching grain boundary network.

In Sec. 5, we present a numerical study of three interconnect geometries. The first is rectangular with a single horizontal grain boundary running through its center. This geometry is simple enough that it is easy to visualize the eigenfunctions and interpret the evolution physically. The second geometry has a more complicated shape as well as a branching grain boundary structure. The evolution is more difficult to visualize, but exhibits very interesting behavior, including a change in sign of the flux of atoms into one of the grain boundary segments midway through the evolution. The third geometry is again rectangular, but has a complicated grain boundary network with two connected components. The break in the network acts as a flux barrier to limit the effective length of the line, inhibiting the development of stress. For all three geometries, we present contour plots of the steady state displacement and stress fields, showing that the largest stress concentrations occur at the ends of each connected component of the grain boundary network, and at corners and junctions where the stress field is singular. We also present a mesh refinement study which indicates third order accuracy in the mesh parameter, and provide numerical evidence that the semigroup operator governing the evolution of normal stress is well defined for initial data in $L^2(\Gamma)$, which slightly strengthens the rigorous result in [15] for initial data in $H^1(\Gamma)$.

The most difficult numerical aspect of this problem involves solving the Lamé equations with interface boundary conditions along grain boundaries. Because the grain growth rate depends on taking two derivatives of the normal stress, it is extremely important that singularities in the stress field near grain boundary junctions be properly resolved. The extended first order system least squares finite element method (X-Fosls) was developed for this purpose, which is described in [17]. Some of the features which make X-Fosls well suited for this problem are as follows: (1) Singularities in the stress field are captured explicitly, and the accuracy of the solution does not degrade near corners and triple junctions. (2) The supports of the singular functions may overlap, and nearly linearly dependent (or fully degenerate, generalized) power solutions corresponding to critical exponents clustered together in the complex plane are stabilized before using them in the finite element space. (3) Very complicated interface boundary conditions can be implemented. (4) The stress and displacement variables may both be modeled using C^0 quadratic elements (plus singular functions) without having to satisfy a Babuška-Brezzi inf-sup condition. (5) There is an a-posteriori measure of the error which indicates where the finite element space has difficulty resolving the solution. See [18] for the use of singular basis functions in FOSLS to solve the steady state diffusion equation with discontinuous coefficients, and [19,20] for analysis of the FOSLS method (without singular functions) for second order elliptic equations and the Stokes system. See [21] for a description of the X-FEM method for branched and intersecting cracks in two-dimensional elasticity.

2 Problem Statement

In this section, we describe a two-dimensional continuum model of electromigration and stress driven grain boundary diffusion in the linear regime of small strain, small grain growth elasticity.

A grain is a region where the atoms are aligned in a regular lattice. A grain boundary is an interface between two grains where the lattice structure be-

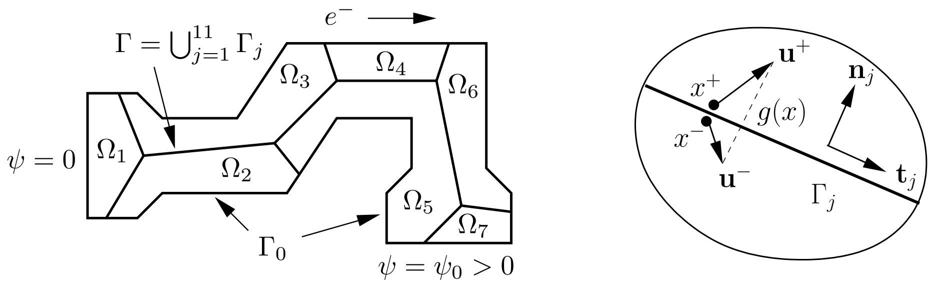

Fig. 1. Left: geometry of an interconnect line. Right: $g(x)$ is the jump in normal component of displacement across Γ at x.

comes disorganized as the lattice alignment changes from one side to the other. In our (continuum) model, we ignore details of lattice alignment and assume all grain boundaries have equivalent properties. In reality, it is likely that the diffusion coefficient for atoms diffusing in the grain boundary will decrease as the grain boundary misorientation approaches zero. This effect can be incorporated into the framework of this paper without difficulty (notably altering L and $\mathcal{F}_i$ in Sec. 3.2), but has been omitted for the sake of clarity.

The grain boundaries are assumed to be fast diffusion paths along which the atoms are much more easily transported by electromigration and chemical potential gradients than in the bulk grains. At each point on the grain boundary, we have a flux J of atoms traveling along the grain boundary. J has units of surface flux ($\text{cm}^{-1}\text{s}^{-1}$), where we consider our two dimensional domain to have a thickness δ in the third dimension. If a portion of the grain boundary has more atoms flowing into it than out, the atoms incorporate themselves into the lattice of the adjacent grains and cause the grains to move apart to make room for the new atoms. At the same time there will be a net flux of atoms out of other regions of the grain boundary, where the adjacent grains move together so as not to leave a gap. Since curvature driven grain boundary motion is not part of our model, we assume that the appropriate fraction of atoms attaches to each side of the grain boundary so that Γ remains fixed in the spatial (stressed) configuration. We do not impose the Young condition requiring that grain boundaries meet at 120° angles since it is not required for well-posedness unless curvature is included as a driving force.

From the point of view of elasticity [22,23], this problem is unusual in that the natural configuration of each grain changes in time as atoms are added to its boundaries while the stressed configuration remains fixed. It is therefore appropriate to adopt an Eulerian picture in which the stress and displacement fields are defined in the spatial configuration and $\mathbf{u}(x) = x - \varphi^{-1}(x)$ instead of $\varphi(x) - x$ for a given deformation φ. The linearized equations of elasticity are the same in the material and Eulerian viewpoints.

We model the interconnect line as a union $\Omega = \bigcup_k \Omega_k$ of disjoint polygonal grains as shown in Fig. 1. We denote the outer boundary (the "walls") of the domain by Γ_0, and the grain boundary network by $\Gamma = \bigcup_{j=1}^{N_\Gamma} \Gamma_j$. Each line segment Γ_j is given an arbitrary orientation (a unit tangent vector $\mathbf{t}_j$) and an arclength parameter s which increases in the $\mathbf{t}_j$ direction. The unit normal $\mathbf{n}_j$ points from right $(-)$ to left $(+)$ facing along $\mathbf{t}_j$. The net grain growth g is defined on Γ as the jump in normal component of displacement across the grain boundary:

$$g(x) := [\mathbf{u}(x^+) - \mathbf{u}(x^-)] \cdot \mathbf{n}_j, \qquad (x \in \Gamma_j). \tag{1}$$

It represents the distance the original grains have separated to accommodate the new material that occupies that space; see Fig. 1. In the Eulerian picture, $g(x) = [\varphi^{-1}(x^-) - \varphi^{-1}(x^+)] \cdot \mathbf{n}$ is the amount that opposite sides of the grain boundary at x would overlap if the grains were allowed to interpenetrate each other to achieve their stress free shapes. This overlap corresponds to new material added during the diffusion process. Note that g evolves as a function defined on Γ as $\mathbf{u}$ evolves on Ω; both Γ and Ω remain *fixed* in time. The sign of g is independent of the orientation chosen for the segment.

In Figure 2, we provide a summary of the equations and boundary conditions in non-dimensional form; see [16,15]. A unit of dimensionless length (x, s, g, $\mathbf{u}$) corresponds to an arbitrarily chosen length scale L ($\sim 1\mu$m). Time (t), stress (σ, η), electrostatic potential (ψ), and flux (J) are respectively measured in multiples of $t_0 = \frac{kTL^3}{\nu_b D_b \Omega_a^2 \mu}$, μ, $\frac{\Omega_a \mu}{|Z^*|e}$ and $\frac{L^2}{\Omega_a t_0}$, where k is Boltzmann's constant, D_b is the diffusion constant for grain boundary diffusion at temperature T, ν_b is the number of participating atoms per unit of grain boundary area, Ω_a is the volume of an atom in the atomic lattice, μ is the shear modulus, Z^*e is a phenomenological effective charge for an ion in the lattice and $e = |e|$ is the elementary electric charge. See [3] for typical values of these parameters.

Equation (2a) of Fig. 2 enforces the requirement that the displacement is zero at the outer walls (passivation). In (3a), we assume the grains do not slide tangentially relative to each other, and define the displacement jump g. In (3b), we enforce the local balance of forces (tractions) across the grain boundary, which together with the no sliding assumption implies that all components of the stress tensor are continuous across grain boundaries. In (3c), we define the normal stress η on the grain boundary, which is well-defined by (3b). Equation (3d) is the main evolution equation, which gives the rate of grain growth in terms of the normal stress and the electrostatic potential. This equation is a consequence of the continuity equation expressing mass conservation, the Einstein-Nernst equation expressing the flux J in terms of the gradient of the chemical potential, the Blech–Herring model of the chemical potential of an atom on a grain boundary [24,16], and the electromigration force. Note that qualitatively, atoms are transported from regions of compression to regions of tension, and travel against the electric field $\mathbf{E} = -\nabla\psi$ in the same direction that electrons flow.

Electric Potential

1. $\nabla^2\psi = 0$
2. $\partial_n\psi = 0$
3. $\psi = 0$
4. $\psi = \psi_0$
5. Grain boundaries are invisible to ψ

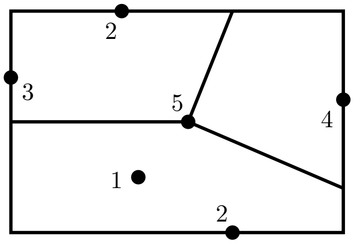

Elasticity and Grain Growth

1a. $\mu\Delta\mathbf{u} + (\lambda+\mu)\nabla(\nabla\cdot\mathbf{u}) = 0$
2a. $\mathbf{u} = 0$
3a. $\mathbf{u}(x^+) - \mathbf{u}(x^-) = g(x)\mathbf{n}$
3b. $\sigma(x^+) = \sigma(x^-)$
3c. $\mathbf{n}\cdot\sigma(x)\mathbf{n} = \eta(x)$
3d. $\partial_t g = -\partial_s^2(\eta+\psi)$ $\begin{cases} J = \partial_s(\eta+\psi) \\ g_t + J_s = 0 \end{cases}$
4a. $g = 0$
4b. $\partial_s(\eta+\psi) = 0$
5a. $g(x_1)\mathbf{n}_1 + g(x_2)\mathbf{n}_2 + g(x_3)\mathbf{n}_3 = 0$
5b. $\eta(x_1) = \eta(x_2) = \eta(x_3)$
5c. $\partial_{s_1}(\eta+\psi) + \partial_{s_2}(\eta+\psi) + \partial_{s_3}(\eta+\psi) = 0$

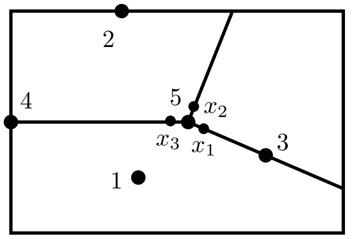

Initial Condition: $g \equiv 0$

Fig. 2. Summary of equations and boundary conditions. Segments are parametrized away from the triple junction in this figure to avoid minus signs.

Equation (4a) follows from (2a) and (3a), but is worth recording as a boundary condition on g. Equation (4b) enforces zero flux at gb–wall junctions: atoms are not allowed to flow in or out of the network where the grain boundary meets passivation, and global mass conservation should hold. Equation (5a) is a compatibility requirement following from (3a): if we start in one grain and follow the jump in displacement around a triple junction, we have to end up with the original displacement when we return. (The point x_i is infinitesimally close to the triple junction on segment i). Equation (5b) enforces chemical potential continuity at triple junctions. Equation (5c) enforces a balance of flux entering and leaving the triple junction.

It will be useful to define the fields $\alpha, \beta, \gamma, \tau$ in terms of the stress tensor σ and displacement field $\mathbf{u} = (u, v, 0)^T$:

$$\alpha = \frac{\sigma_{11}+\sigma_{22}}{2\mu}, \quad \gamma = \frac{\sigma_{22}-\sigma_{11}}{2\mu}, \quad \tau = \frac{\sigma_{12}}{\mu}, \quad \beta = \frac{2}{\varkappa+1}(v_x - u_y), \tag{2}$$

where $\varkappa = 3 - 4\nu$ in plane strain and $0 \le \nu \le 1/2$ is the Poisson ratio. The energy density is given by $E = \sigma_{ij}\epsilon_{ij} = \mu\left(\frac{\varkappa-1}{2}\alpha^2 + \gamma^2 + \tau^2\right)$.

3 Theory

In this section, we summarize those aspects of the theory of electromigration and stress driven grain boundary diffusion necessary for developing our numerical method; see [15,16] for further details. Key challenges include: finding a way to organize the equations and boundary conditions so that mathematical questions such as well-posedness can be addressed; determining the role of singularities in the stress field near corners and junctions where derivatives of the stress field enter as boundary conditions; and dealing with the non-local nature of expressions which relate the displacement jump g to the normal stress η — placing local constraints on one imposes (rather awkward) global constraints on the other via the Lamé equations. Our approach is to recast the problem as an ordinary differential equation on a Hilbert space, writing the equation in terms of the normal stress η and absorbing all the boundary conditions into the operators. The equation takes the form $\eta_t = SL(\eta + \psi)$, so we begin by defining S, L, and several related operators.

3.1 The operators S and B

The operator S is a type of Dirichlet to Neumann map which takes a specified grain growth function g and returns the corresponding normal stress η on the grain boundary. S is defined rigorously in [15] as the inverse of the operator

$$B : L^2(\Gamma) \to L^2(\Gamma), \qquad \text{(normal stress to grain growth map)}. \tag{3}$$

If $\mathbf{u}$ solves the grain boundary normal stress problem (defined below) for a given normal stress η (see Fig. 3), then $B\eta$ is the jump in normal component of displacement across the grain boundary:

$$(B\eta)(x) = [\mathbf{u}(x^+) - \mathbf{u}(x^-)] \cdot \mathbf{n}_j, \qquad (x \in \Gamma_j). \tag{4}$$

This definition is independent of the orientation chosen for each segment. It is shown in [15], that B is self-adjoint, negative and compact, while S is self-adjoint, negative, unbounded, closed and densely defined.

Definition 1 (grain boundary normal stress problem) *Given a function $\eta \in L^2(\Gamma)$, find the displacement field $\mathbf{u} \in H^1(\Omega)^2$ satisfying the Lamé equations $\mu\Delta\mathbf{u} + (\lambda+\mu)\nabla(\nabla\cdot\mathbf{u}) = 0$ in the interior of each grain subject to the boundary conditions*

$$\begin{aligned} \mathbf{u}(x) &= \mathbf{0}, && (x \in \Gamma_0), \\ [\mathbf{u}(x^+) - \mathbf{u}(x^-)] \cdot \mathbf{t}_j &= 0, && (x \in \Gamma_j), \\ [\sigma(x^+) - \sigma(x^-)]\mathbf{n}_j &= \mathbf{0}, && (x \in \Gamma_j), \\ \mathbf{n}_j \cdot \sigma(x)\mathbf{n}_j &= \eta(x), && (x \in \Gamma_j). \end{aligned} \tag{5}$$

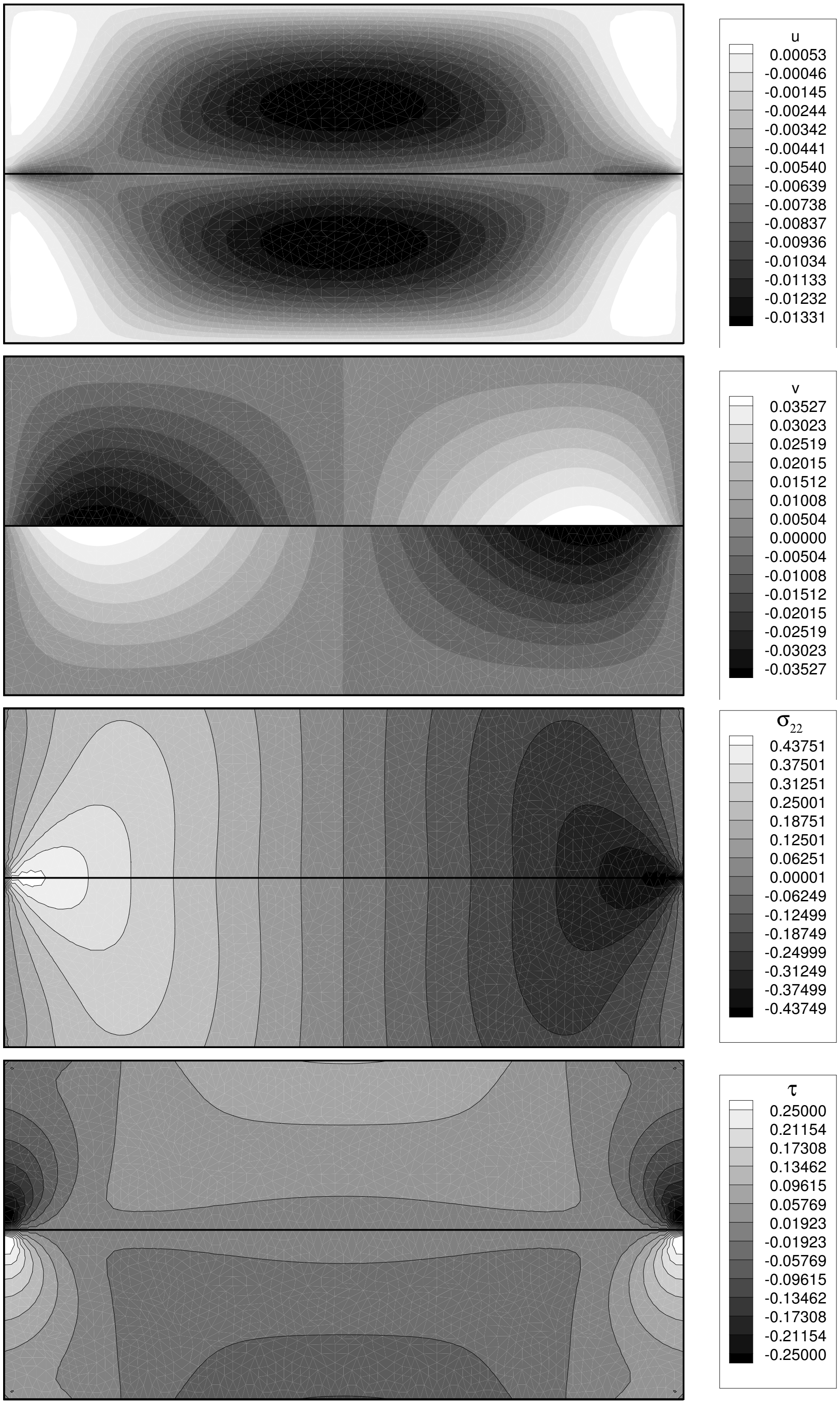

Fig. 3. Displacement and stress components u, v, σ_{22}, σ_{12} corresponding to the normal stress $\eta(x) = (1-x)/2$ along the grain boundary $(0 \le x \le 2,\ y = 0)$; $g = B\eta$ is given by $g(x) = v(x, 0^+) - v(x, 0^-)$. (Poisson ratio 0.35, plane strain).

To make sense of the boundary conditions (5) for an arbitrary $\eta \in L^2(\Gamma)$, a suitable notion of weak solution to the grain boundary normal stress problem must be defined; see [15]. There it is shown that for certain “degenerate” grain boundary networks, additional compatibility conditions must be satisfied by η for a solution $\mathbf{u}$ to exist, and when it does exist, it is not unique. In the degenerate case, the operator B (defined appropriately to deal with existence and uniqueness) is not injective, and S and B are pseudo-inverses of each other, sharing a finite dimensional kernel. Degeneracy occurs when stress free (grain by grain) infinitesimal rigid body motions exist which satisfy (5) with $\eta \equiv 0$, i.e. which are zero at the outer walls and satisfy a “no sliding” condition across grain boundaries. In all cases, grain boundary diffusion causes the stress field to evolve to a steady state distribution which balances the electromigration force along grain boundaries; however, in the degenerate case, the diffusion process continues to transfer material around the grains so that the displacements grow steadily without bound along stress free modes. The picture is suggestive of continental drift in plate tectonics, although the physical mechanism is completely different. An algorithm for finding the degeneracies of any grain boundary network is presented in [15], where it is shown that degeneracy is a consequence of pathologies such as junction angles greater than 180° or a large number of quadruple (or higher) order junctions. Physically, such angles would not occur at a triple junction due to curvature driven grain boundary motion [7]. In this paper, we explicitly assume we are working in the non-degenerate case, so that B is injective, S is surjective, and the grain boundary normal stress problem is uniquely solvable for any $\eta \in L^2(\Gamma)$.

3.2 The operators L and A

The operator L is the negative of the second derivative operator with respect to arclength on each grain boundary segment. If η is twice continuously differentiable and satisfies the boundary conditions

$$\begin{matrix} \eta \text{ is continuous at } x_i \\ \mathcal{F}_i\eta = 0 \end{matrix} \qquad (i \text{ any junction label}), \tag{6}$$

then the restriction of $L\eta$ to the interior of Γ_j is given by

$$L\eta(x) = -\frac{\partial^2 \eta}{\partial s^2}, \qquad (x \in \Gamma_j^o). \tag{7}$$

Here $\mathcal{F}_i\eta$ is given by

$$\mathcal{F}_i\eta = (-1)^{k_i}\partial_s\eta(x_i), \qquad (x_i \text{ a gb–wall junction}), \tag{8}$$

$$\mathcal{F}_i\eta = \sum_{j=1}^{3}(-1)^{k_i^j}\partial_s\eta(x_i^j), \quad (x_i \text{ a triple gb junction}), \tag{9}$$

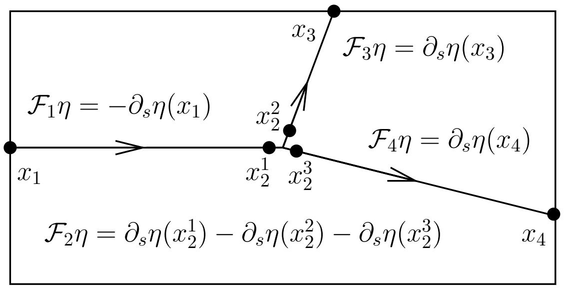

Fig. 4. $\mathcal{F}_i\eta$ is a sum over segments incident to junction i of slopes $\pm\partial_s\eta$.

where x_i^j is infinitesimally close to junction x_i on segment j and k_i^j is 0 or 1 depending on whether segment j is parameterized toward or away from x_i; see Figure 4. We recall from Section 2 that if η is the normal stress and ψ is the electrostatic potential then the flux of atoms along the grain boundary is given by $J = \partial_s(\eta + \psi)$; thus the flux into junction i is given by $\mathcal{F}_i(\eta + \psi)$.

It is shown in [15] that L is a self-adjoint, positive operator with d dimensional kernel, where d is the number of connected components Γ_{J_k} of the grain boundary network. Here $J_1, \ldots, J_d$ are sets of segment indices corresponding to each connected component. An orthonormal basis for $\ker(L)$ consists of functions $e_k(x)$ which are constant on Γ_{J_k} and zero on all other components. Since the connected components are separated from each other, the e_k are continuous functions on Γ. We define the operator A and the projection P by

$$A = L + \sum_1^d (\cdot, e_k)e_k, \qquad P = I - \sum_1^d (\cdot, e_k)e_k. \tag{10}$$

P is the orthogonal projection onto the subspace

$$\ker(L)^\perp \;=\; \Big\{ f \in L^2(\Gamma) \;:\; \int_{\Gamma_{J_k}} f\,ds = 0,\; 1 \le k \le d \Big\}. \tag{11}$$

L and A are related via

$$L = AP = PA. \tag{12}$$

$A^{1/2}$ is an isomorphism from $H^1(\Gamma)$ onto $L^2(\Gamma)$, where $H^1(\Gamma)$ consists of all absolutely continuous functions on the grain boundary such that the (segment by segment) derivative with respect to arclength belongs to $L^2(\Gamma)$; see [15].

3.3 The semigroup $\{E_t : t \ge 0\}$

Referring back to Figure 2, the evolution of the jump in displacement g is governed by the equation

$$g_t = L(\eta + \psi) = L(Sg + \psi). \tag{13}$$

Applying S, we obtain an equation for the evolution of the normal stress:

$$\eta_t = SL(\eta + \psi). \tag{14}$$

The solution to this equation with initial condition η_0 (usually 0) is given by

$$\eta(t) = E_t(\eta_0 + \psi) - \psi, \qquad (t \geq 0) \tag{15}$$

where E_t is the analytic semigroup [25,26] on $H^1(\Gamma)$ generated by SL. We define the (non-orthogonal) projection Q via

$$Qw = \begin{cases} w & w \in \text{range}(SL), \\ 0 & w \in \ker(SL). \end{cases} \tag{16}$$

It is shown in [15] that $E_t \to I - Q$ in the $H^1(\Gamma)$ norm as $t \to \infty$. Thus the steady state stress distribution is given by

$$\eta_{\text{steady}} = (I - Q)\eta_0 - Q\psi. \tag{17}$$

The fact that $[\eta(t) + \psi] \in \text{range}(E_t) \subset \mathcal{D}(SL)$ for $t > 0$ ensures that boundary conditions (4b), (5b) and (5c) from Figure 2 hold for $t > 0$. Boundary conditions (4a) and (5a) follow from the fact that we obtain g from $\mathbf{u}$ via (4). The remaining equations are built into the grain boundary normal stress problem implicit in the definition of S and B. Since we are working in the non-degenerate case, the displacement jump may be obtained from (15) via

$$g(t) = B\eta(t), \qquad (t \geq 0). \tag{18}$$

It is proved in [15] that there is a Riesz basis $\{\phi_k\}_{k=1}^{\infty}$ for $H^1(\Gamma)$ and a non-increasing, unbounded sequence of numbers $\lambda_k \leq 0$ such that $SL\phi_k = \lambda_k\phi_k$. (A Riesz basis is a basis equivalent to an orthonormal basis [27]). We may take $\phi_k = e_k$ for $(1 \leq k \leq d)$ since these span $\ker(SL)$ in the non-degenerate case. There also exist $\phi_k^* \in L^2(\Gamma)$ such that $LS\phi_k^* = \lambda_k\phi_k^*$ and $(\phi_i, \phi_j^*)_{L^2(\Gamma)} = \delta_{ij}$. The ϕ_k^* need not belong to $H^1(\Gamma)$ due to discontinuities and infinite slopes at junctions. For $\eta \in H^1(\Gamma)$ the expansions

$$\eta = \sum_{k=1}^{\infty} a_k\phi_k, \qquad E_t\eta = \sum_{k=1}^{\infty} a_k e^{\lambda_k t}\phi_k, \qquad a_k = (\eta, \phi_k^*)_{L^2(\Gamma)} \tag{19}$$

hold in $H^1(\Gamma)$. Although the $L^2(\Gamma)$ norm of ϕ_k^* diverges as $k \to \infty$, the inner products a_k in (19) do not; they are square summable when η belongs to $H^1(\Gamma)$. For computational convenience, we re-normalize the ϕ_k so that they are unit vectors in $L^2(\Gamma)$ instead of in $H^1(\Gamma)$:

$$\|\phi_k\|_{L^2(\Gamma)} = 1, \qquad (\phi_i, \phi_j^*)_{L^2(\Gamma)} = \delta_{ij}. \tag{20}$$

Although the ϕ_k cease to be a basis for $H^1(\Gamma)$, this choice of normalization does not affect the $H^1(\Gamma)$ convergence of the expansions (19) since the ϕ_k^* (and hence the a_k) have been correspondingly rescaled.

3.4 A compact pseudo-inverse for computing eigenfunctions

The expansions (19) are the basis of our numerical method. In order to use them, we need a method of computing the ϕ_k, ϕ_k^* and λ_k. In [15], it is shown that the following pseudo-inverse relationship holds:

$$K := \mathrm{pinv}(SL) = QA^{-1}BQ. \tag{21}$$

Here Q is defined as above as the projection along $\ker(SL)$ onto $\mathrm{range}(SL)$, and the meaning of (21) is

$$SLK = KSL = Q. \tag{22}$$

Thus K and SL have the same kernel, range, and eigenfunctions with reciprocal (or zero) eigenvalues:

$$K\phi_k = \mu_k \phi_k, \qquad \mu_k = \begin{cases} 0 & 1 \le k \le d, \\ \lambda_k^{-1} & k > d. \end{cases} \tag{23}$$

We remark that the pseudo-inverse is normally obtained from the SVD by inverting non-zero singular values and exchanging left and right singular vectors. Since we are interested in finding eigenfunction expansions rather than solving least squares problems, we invert non-zero eigenvalues in the diagonalization of SL instead. If SL were self-adjoint, the two definitions would coincide.

3.5 Singularities and well-posedness

The singularities which arise in the components of the stress tensor near corners and grain boundary junctions are asymptotically sums of power solutions (of the form $r^\lambda \phi(\theta)$ in local polar coordinates on each grain touching the junction), and satisfy *homogeneous* interface boundary conditions to the Lamé system; see [16,28]. In the current case, the boundary conditions for the elasticity problem along the grain boundary are that the normal stress $\mathbf{n} \cdot \sigma \mathbf{n}$ is prescribed independently on each side to be equal to η, and the tangential displacement $\mathbf{u} \cdot \mathbf{t}$ and shear stress $\mathbf{t} \cdot \sigma \mathbf{n}$ is continuous across the interface. As a result, the singular part of the solution near a given junction satisfies $\eta = 0$ along the grain boundaries entering the junction. Although a different combination of the components of the stress tensor will generally diverge along

Γ, $\mathbf{n} \cdot \sigma \mathbf{n}$ will remain finite and well-behaved, and the various flux boundary conditions in Fig. 2 describe quantities which remain finite in spite of the singularities. The corresponding displacement jump g will also remain finite, although it will generally exhibit infinite slopes at the endpoints of the grain boundary segments.

4 Numerical Algorithm for Grain Boundary Diffusion

Because A^{-1}, B and K are compact operators on $L^2(\Gamma)$, they are well approximated by finite rank operators, making it possible to compute them numerically. Once these have been found, we use standard numerical linear algebra methods to approximate λ_k, ϕ_k, and ϕ_k^* in the expansion (19), which immediately gives the evolution at any time $t \geq 0$.

To compute B, we must repeatedly solve the grain boundary normal stress problem; see Sec. 4.1. This is computationally equivalent to taking a few hundred timesteps using an explicit scheme. The computations presented in this paper range from taking a few seconds to several minutes on a typical 1 GHz single processor workstation. We choose a mesh parameter h and divide each grain boundary segment Γ_j into equal subsegments (line elements) of length $h_j \leq h$. The segments of the outer boundary Γ_0 are similarly subdivided, and each grain is triangulated using the endpoints of the line elements as the exterior vertices of the triangulation. See Fig. 5.

We will make use of two subspaces of $L^2(\Gamma)$ on the grain boundary. The first consists of all continuous functions which are quadratic on any line element.

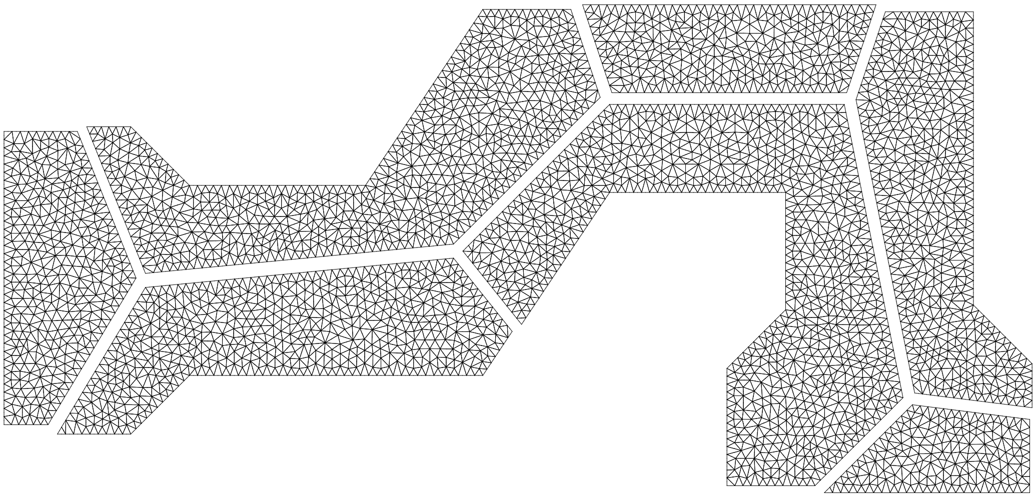

Fig. 5. Each grain is triangulated separately, leading to an unstructured mesh with duplicate nodes along grain boundaries and triple nodes at triple junctions.

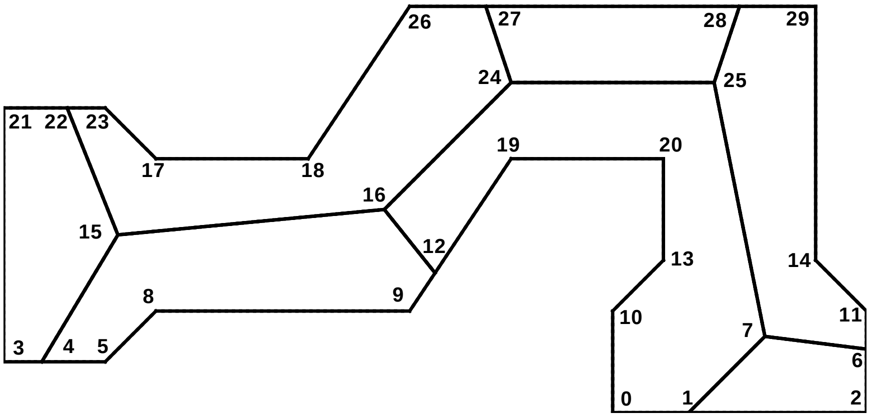

Fig. 6. Corners and grain boundary junctions are numbered arbitrarily.

The standard basis functions for one dimensional quadratic C^0 finite elements are used. Enumerating the nodes x_i (at endpoints and midpoints of grain boundary line elements) in some way, we obtain a basis $\{\varepsilon_i\}_{i=1}^m$ for this space such that $\varepsilon_i(x_j) = \delta_{ij}$. Note that if x_i is a triple junction, then the support of ε_i consists of the three line elements incident on x_i; double and triple nodes are *not* used in the one dimensional network described here, even though they are used in the ambient two dimensional triangulation. The normal stress η will be modeled in this space.

The second space of functions is largely the same as the first, with two exceptions: several special basis functions are added to capture singular behavior, and the ε_i corresponding to junctions are removed from the basis set. We denote the basis functions for this space by $\{q_j\}_{j=1}^n$. For each non-singular q_j there is an i such that $q_j(x) = \varepsilon_i(x)$ on Γ, and for each non-junction x_i there is a j such that $q_j(x) = \varepsilon_i(x)$ on Γ. The discontinuities in g at triple (or higher order) junctions are special cases of power solutions with exponent 0; they are modeled as singular functions as well. Normally $n \geq m$ since we adjoin at least one singular function to each junction. The displacement jump g will be modeled in this space.

In Fig. 7, we show the basis functions q_j for the geometry of Fig. 6 which are non-zero on the segment from junction 24 to 27. There are 12 line elements on this segment. Each of the eight special basis functions shown is defined piecewise: near the junction it is a power solution of the form $\mathrm{Re}\{cr^\lambda\}$; far from the junction it is zero; and between the two regions it is quadratic. The exponents involved are $\lambda = 0$, .7830, .9018, $2.140 \pm .567i$ at junction 24 and $\lambda = .6564$, $2.017 \pm .466i$ at junction 27 (computed to machine precision in the code). The $\lambda = 0$ singular function is discontinuous at junction 24 to enforce rigid body separation of the three grains with no grain boundary sliding; see Eq. (5a) of Fig. 2. There are two remaining displacement degrees of freedom in the two dimensional finite element space which allow lock-step rigid body motion of the three grains here, but they do not affect the displacement jump g.

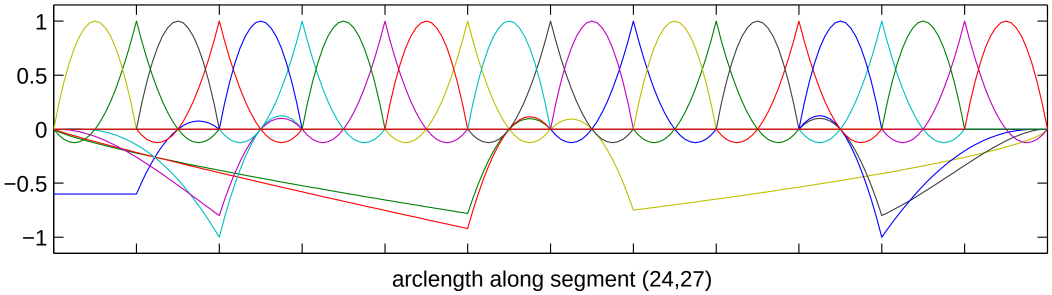

Fig. 7. The basis functions q_j are continuous and piecewise quadratic/self-similar.

There are several reasons we have chosen to use different spaces for η and g. The main objection to doing so is that B and A^{-1} are each self-adjoint, negative or positive definite operators on $L^2(\Gamma)$, so it would be nice to require that their numerical approximations also have these properties. This would guarantee that various matrices which arise in the algorithm are invertible, and would ensure the correct qualitative behavior of the semigroup operator E_t in (19). However, to faithfully approximate B as a self-adjoint operator on a finite dimensional subspace $H_h \subset L^2(\Gamma)$, the exact operator B must leave H_h approximately invariant. This would require that H_h contain functions which are discontinuous at junctions, and that we be able to solve the grain boundary normal stress problem accurately for discontinuous η. But the theory of grain boundary diffusion outlined in Sec. 3 is most naturally carried out with $\eta \in H^1(\Gamma)$, which implies η is continuous. The eigenfunctions of $K = QA^{-1}BQ$ all belong to $H^1(\Gamma)$ since Qf differs from f by at most a constant on each grain boundary component and range$(A^{-1}) \subset H^1(\Gamma)$.

The composition $A^{-1}B$ leaves $H^1(\Gamma)$ invariant even though B does not (due to discontinuities and infinite slopes in $B\eta$). Our choice of spaces for η and g is the finite dimensional analog of modeling $\eta \in H^1(\Gamma)$ and $g \in B(H^1(\Gamma))$ in the continuous problem. We will see that

$$A^{-1}B = (E^{-1}\widetilde{M})(B) = (E^{-1}M)(M^{-1}\widetilde{M}B), \tag{24}$$

where E, $\widetilde{M}$, and M are stiffness and mass matrices defined in Section 4.3. The first way of grouping the operators in (24) emphasizes the *accuracy* of the method, where we take full advantage of the theory of asymptotic behavior of elliptic systems near corners and interface junctions [28,29] when solving the grain boundary normal stress problem. B and A^{-1} are respectively $n \times m$ and $m \times n$ matrices, and we model $\eta \in \text{span}\{\varepsilon_i\}_{i=1}^m$ and $g \in \text{span}\{q_j\}_{j=1}^n$. But the second way of grouping the operators shows that we do not have to sacrifice a-priori guarantees of algorithmic correctness which rely on the fact that $A^{-1}B$ is a product of self-adjoint positive/negative definite operators: $E^{-1}M$ is self-adjoint and positive definite with respect to the $L^2(\Gamma)$ inner product on span$\{\varepsilon_i\}$, and we will show that it is possible to symmetrize B so that $M^{-1}\widetilde{M}B$ is self-adjoint and negative definite on this space.

B was defined in equation (4) as the operator which takes a specified normal stress $\eta \in L^2(\Gamma)$, solves the grain boundary normal stress problem for the displacement field $\mathbf{u}$, and returns the jump g in the normal component of $\mathbf{u}$ across Γ. Given a normal stress $\eta = \sum_1^m \eta_i \varepsilon_i$, we use the X-Fosls method described in [17] to solve for $\mathbf{u}$ on the entire two dimensional finite element space. We then compute $g = \sum_1^n g_j q_j$ on the grain boundary

$$g = [\mathbf{u}(x^+) - \mathbf{u}(x^-)] \cdot \mathbf{n}_j \qquad (x \in \Gamma_j). \tag{25}$$

The degrees of freedom available for discontinuity in the displacement field across Γ in the two dimensional finite element space coincide precisely with the basis functions q_j. Extracting g from the solution w is straightforward, and does not involve projections or any loss of information. This procedure produces an approximation to B as a mapping from $\mathbb{R}^m \to \mathbb{R}^n$ corresponding to the bases $\{\varepsilon_i\}$, $\{q_j\}$ for normal stress and displacement jump.

In X-Fosls [17], the first several terms in the asymptotic expansion of the behavior of the Lamé equations near corners and junctions are computed using semi-analytic methods [30], and are adjoined to the finite element space; see Fig. 8. Near the corner or junction, the singular basis functions are self-similar power solutions, with components of the form

$$w_j(r, \theta) = r^{\lambda + t_j} \phi_j(\theta), \tag{26}$$

where $w = (u, v, \alpha, \beta, \gamma, \tau)^T$ and $(t_j) = (0, 0, -1, -1, -1, -1)$; see Eq. (2) and Fig. 9. Each singular basis function has a "fringe region" consisting of a layer of triangles (straddling the fringe radius) on which it transitions to zero. The fringe radii of different singular basis functions may be different, and their supports may overlap one another, as long as they do not extend out so far as

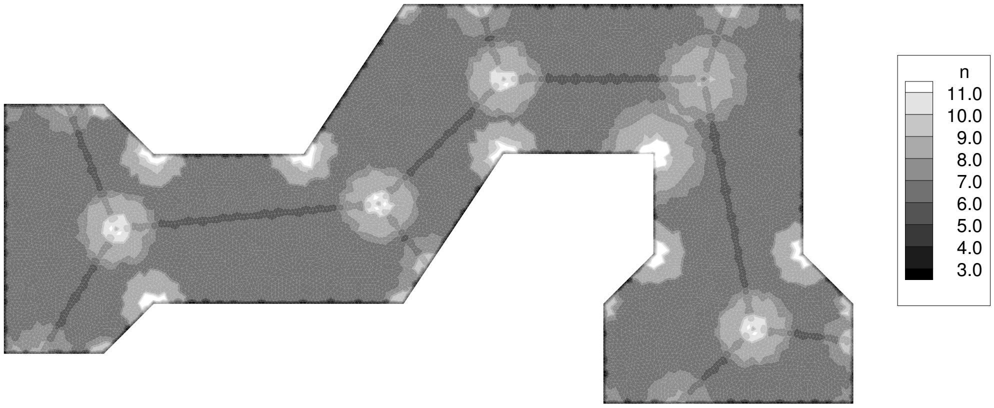

Fig. 8. Number of degrees of freedom that affect $w = (u, v, \alpha, \beta, \gamma, \tau)^T$ at each node. 101 extra basis functions are used here to capture asymptotic behavior.

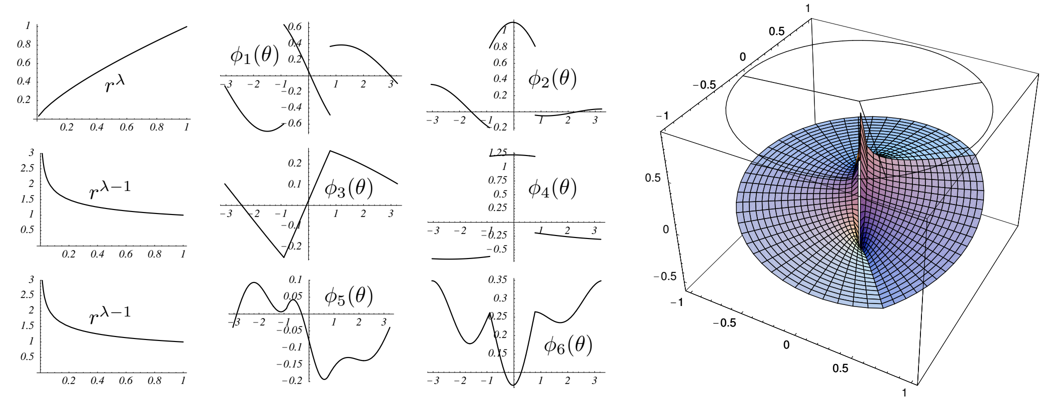

Fig. 9. *Left:* Radial and angular dependence of one of the power solutions $w_j(r,\theta) = r^{\lambda+t_j}\phi_j(\theta)$ near jcn. 16 of Fig. 6 ($\lambda = 0.7474$). *Right:* 3d plot of $\alpha = w_3$.

to intersect distant walls or grain boundaries. The key property that makes it easier to augment the finite element space with singular functions in least squares finite elements over Galerkin finite elements is that inner products involving a singular function only involve integration in the fringe region, where it is well-behaved; thus sophisticated quadrature schemes dealing with the singularity are unnecessary. See [17,16,18] and Eq. (29) below.

The characteristic exponents λ in (26) which arise in this problem are often complex. Moreover, they can become clustered together or even coalesce in the complex plane at certain critical angles. In the former case the power solutions can be nearly linearly dependent, and in the latter case generalized power solutions with logarithm terms may arise in the asymptotic expansion as well. In X-Fosls, nearly degenerate (or generalized) power solutions corresponding to such a cluster are stabilized before they are included in the finite element basis to avoid unnecessary ill-conditioning; see [17,16].

Each triangle of the mesh in Fig. 5 has six quadratic functions defined on it (the components of w), plus any singular functions which contain the triangle in their "near" regions. We impose boundary conditions absolutely, minimizing the equation residual over all functions in the affine subspace satisfying the boundary conditions. This is why there are fewer degrees of freedom along walls and grain boundaries in Fig. 8. More explicitly, we write the equations of linear elasticity $\mu\Delta\mathbf{u} + (\lambda+\mu)\nabla(\nabla\cdot\mathbf{u}) + \mathbf{F} = 0$ as an equivalent first order system

$$L(\partial_x, \partial_y)w = f \tag{27}$$

and seek the minimizer of the functional

$$J[w] = \frac{1}{2}\|Lw - f\|^2 = \frac{1}{2}a(w,w) - b(w,f) + \frac{1}{2}\|f\|^2 \tag{28}$$

over the affine subspace of functions w satisfying the boundary conditions. Here $a(w,v) = (Lw, Lv)$, $b(w,f) = (Lw,f)$, and $(f,g) = \sum_i \int_\Omega f_i g_i \, dA$. Taking the first variation, we find that the solution w satisfies

$$a(w, v) = b(v, f) \tag{29}$$

for all v satisfying *homogeneous* boundary conditions (so as not to take w out of the affine subspace). Note that because the singular functions satisfy $Lw \equiv 0$ in the near and far regions, singular components of w and v only contribute to (29) in their fringe regions. The operator L in (27) is given by

$$L(\partial_x, \partial_y) = \begin{pmatrix} \partial_x & -\partial_y & 0 & 0 & 1 & 0 \\ \partial_y & \partial_x & 0 & 0 & 0 & -1 \\ -\partial_y & \partial_x & 0 & -\frac{\varkappa+1}{2} & 0 & 0 \\ \partial_x & \partial_y & -\frac{\varkappa-1}{2} & 0 & 0 & 0 \\ 0 & 0 & \partial_x & 0 & -\partial_x & \partial_y \\ 0 & 0 & \partial_y & 0 & \partial_y & \partial_x \\ 0 & 0 & \partial_x & -\partial_y & 0 & 0 \\ 0 & 0 & \partial_y & \partial_x & 0 & 0 \end{pmatrix}, \quad f = -\mu^{-1} \begin{pmatrix} 0 \\ 0 \\ 0 \\ 0 \\ F_1 \\ F_2 \\ \frac{2}{\varkappa+1} F_1 \\ \frac{2}{\varkappa+1} F_2 \end{pmatrix}. \tag{30}$$

The last two equations follow from the first six, but including them improves the condition number of the stiffness matrix. To our knowledge, this reduction to a first order system has not been used before; note that α and β satisfy the Cauchy-Riemann equations, the coefficients of the operator L do not diverge as the material becomes incompressible ($\varkappa \to 1$), and this system is equivalent to the Stokes equations when $\varkappa = 1$. See [17] for further details.

Since Γ is essentially one dimensional, m and n are much smaller than the number of degrees of freedom in the two-dimensional mesh used to solve the grain boundary normal stress problem. Thus it is not particularly expensive to store the matrix B as a dense matrix. The X-Fosls method leads to a linear system $Aw = -R\eta$, where A is a sparse, symmetric, positive definite $N \times N$ matrix and R is a sparse $N \times m$ matrix. Since there are no body forces, f is zero in (29), but the non-zero boundary conditions embedded in w are moved to the right hand side when solving for the unknown components of w. Much work has been done in developing iterative methods such as preconditioned conjugate gradients or multigrid to rapidly solve such equations. In our case, however, we have to solve the linear system m times in order to compute B, so it is actually better to do a sparse Cholesky factorization once, and then repeatedly backsolve for each right hand side. We have used a variant of the min-degree heuristic known as *symamd* [31] to re-order the matrix for our fast sparse Cholesky solver. We typically find that the Cholesky factor L of the re-ordered matrix A has only 4–5 times as many nonzero entries as the lower triangle of $A = LL^T$; thus once L is found, it takes only 4–5 times as long to solve $Ax = b$ for a given b as it takes to compute Ax for a given x. See [16] for details of our sparse Cholesky implementation. The stiffness matrix A here is unrelated to the grain boundary operator A outside this section.

4.2 Data structures for the branching grain boundary network

A general grain boundary network lacks a natural ordering for the nodes on the grain boundary. As a result, it is important to develop data structures which can be used to easily extract and manipulate grain boundary variables. The normal stress basis functions ε_i are in one-to-one correspondence with grain boundary nodes. We enumerate junctions first, and then sweep through each grain boundary segment to obtain the interior nodes. The displacement jump variables q_j are enumerated by first listing all singular functions (such as the eight shown in Fig. 7), and then sweeping through the grain boundary segments as in the case above.

Omitting details, we maintain several interwoven data structures that allow us to determine the index of the nodes in the ambient two dimensional finite element space which coincide with a given grain boundary node, determine which one is on the right or left, and determine which self-similar basis functions contain the node in their support. We also have data structures to go back the other way, i.e. nodes and triangles of the large finite element space carry information about whether they are on a grain boundary, what the boundary conditions look like there, which singular basis elements affect them, etc. The performance overhead of such book-keeping devices is negligible, and once the low level implementation is in place, they are straightforward to use. These data structures are implemented using vectors and maps in C++ and arrays and hashes in Perl. We use Perl to process the geometry, set up the boundary conditions, and triangulate the mesh; we use C++ to compute singular behavior near junctions, set up the stiffness matrix, and compute the grain boundary operators A^{-1} and B; we use Matlab to compute K and the semigroup operator E_t; and we use C++ to compute the displacement and stress fields corresponding to the normal stress at various times in the evolution.

We also need some way of visualizing functions on the grain boundary. To visualize the displacement jump g, one convenient approach is to show the natural (unstressed) state of each grain by plotting the two curves $x - C\mathbf{u}(x^{\pm})$ as x ranges over Γ for some scaling factor C. This is useful for obtaining a global picture of the way g changes from segment to segment. To get more detailed information about g, and to visualize a function such as η which is not a jump in displacement, it is useful to look at the restriction of the function to various grain boundary segments. This involves unscrambling the variables by constructing a visualization matrix for each segment with columns that

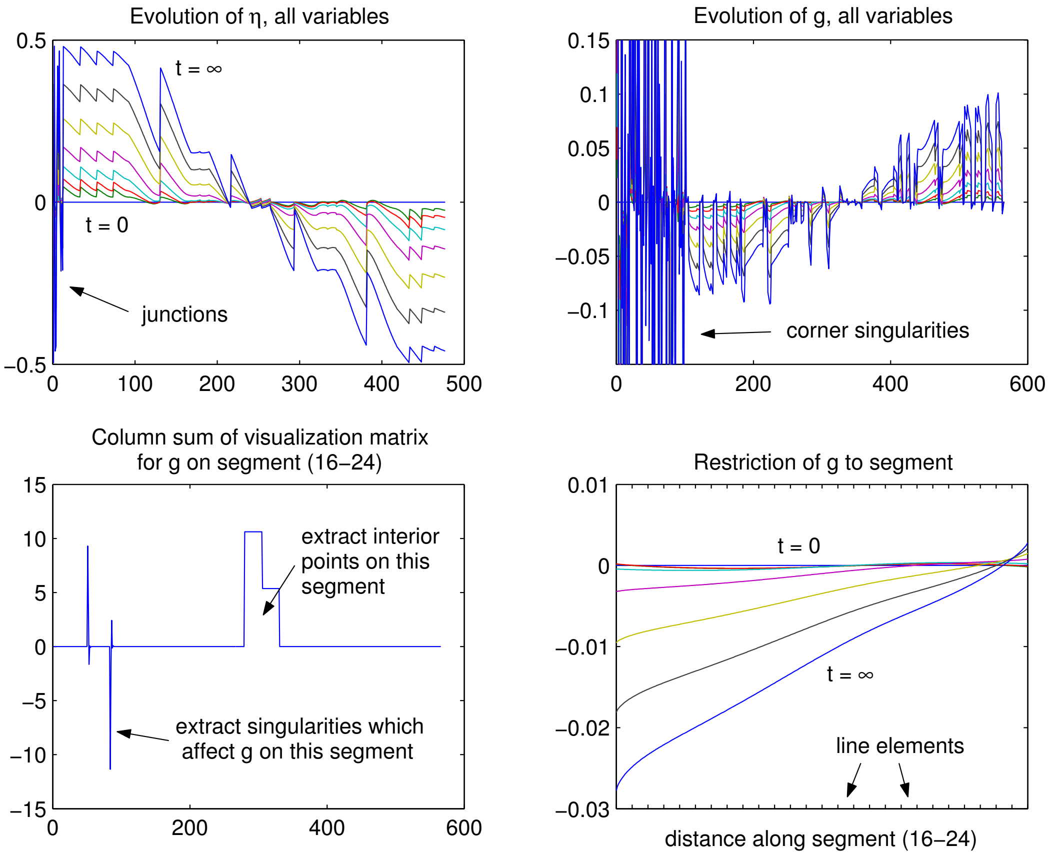

Fig. 10. Plotting a function on a segment involves unscrambling the variables and evaluating quadratic and singular functions at closely spaced points.

correspond to the scrambled variables and rows which correspond to function values at equally spaced points along the segment. The spacing is usually taken to be smaller than the length of a line element in order to resolve the quadratic and singular functions.

In Fig. 10, we show a time evolution of η and g for the geometry of Figure 6 at (dimensionless) times $t = .03, .06, .12, .24, .48, .96, \infty$. Segment (16–24) is oriented from junction 16 to junction 24 in Fig. 6. Sixteen points are used within each line element to view quadratic and singular behavior, which is useful, for example, in Fig. 11. The large amplitude of the singular basis coefficients is an artifact of their normalization in X-Fosls.

4.3 Computing A^{-1}*: the Poisson equation on the network*

Multiplying $L\eta = g$ by a test function φ, integrating by parts on each segment, and using the boundary conditions (6), we obtain the weak form of the Poisson problem on the grain boundary network:

$$\int_\Gamma (\partial_s\varphi)(\partial_s\eta)\,ds = \int_\Gamma \varphi g\,ds, \qquad (\varphi \in H^1(\Gamma)). \tag{31}$$

We write $g = \sum_1^n g_j q_j$, $\eta = \sum_1^m \eta_i \varepsilon_i$ and let φ range over the ε_i to obtain the system of equations $E\eta = \widetilde{M}g$, where

$$E_{ij} = (\partial_s\varepsilon_i, \partial_s\varepsilon_j)_{L^2}, \quad \widetilde{M}_{ij} = (\varepsilon_i, q_j)_{L^2}, \quad M_{ij} = (\varepsilon_i, \varepsilon_j)_{L^2}. \tag{32}$$

To avoid excessive notation, we have identified $\mathbb{R}^m$ with $\operatorname{span}\{\varepsilon_i\} \subset H^1(\Gamma)$ and $\mathbb{R}^n$ with $\operatorname{span}\{q_j\} \subset L^2(\Gamma)$. Note that the stiffness matrix E is $m \times m$ while the mass matrix $\widetilde{M}$ is $m \times n$. All entries of $\widetilde{M}$ are computed analytically, including the entries that involve the integration of a power solution q_j against a piecewise quadratic ε_i. Except for the nodes at branching junctions, E and M are standard stiffness and mass matrices for one dimensional C^0 quadratic finite elements. Moreover, $\widetilde{M}$ largely agrees with M since most of the ε_i and q_j coincide (relabeling indices as necessary, excluding singular q_j and gb–wall ε_i). This is because we are able to use the same elements for both stress and displacement in the ambient elasticity problem — there is no Babuška-Brezzi inf-sup condition [32,33] in X-Fosls to prevent the simultaneous use of continuous spaces for both stress and displacement.

Proceeding similarly, the solution of $A\eta = g$ must satisfy

$$(\partial_s\eta, \partial_s\varphi)_{L^2} + \sum_{k=1}^d (\eta, e_k)_{L^2}(e_k, \varphi)_{L^2} = (g, \varphi)_{L^2}, \qquad (\varphi \in H^1(\Gamma)). \tag{33}$$

We decompose the m nodes on Γ into d disjoint sets corresponding to the connected components Γ_{J_k}. This is easily done using depth first search, for example. Next we form the $m \times d$ matrix e such that

$$e_{ik} = \begin{cases} |\Gamma_{J_k}|^{-1/2} & \text{node } i \text{ belongs to } \Gamma_{J_k} \\ 0 & \text{otherwise.} \end{cases} \tag{34}$$

Note that the columns of e are orthogonal unit vectors in $L^2(\Gamma)$, i.e. $e^T M e = I_d$. The matrix representing A^{-1} with respect to the bases $\{\varepsilon_i\}$, $\{q_j\}$ is given by

$$A^{-1} = \widetilde{E}^{-1}\widetilde{M}, \qquad (\widetilde{E} = E + Me\,e^T M) \tag{35}$$

where e^T is the matrix transpose of e. By (33), if $g \in \operatorname{span}\{q_j\}$, $\eta = A^{-1}_{\text{matrix}}g$, and $\eta_e = A^{-1}_{\text{exact}}g$, then $\eta - \eta_e$ is orthogonal to every $\varphi \in \operatorname{span}\{\varepsilon_i\}$ with respect to the inner product

$$(\eta, \xi)_A = (A\eta, \xi)_{L^2} = (A^{1/2}\eta, A^{1/2}\xi)_{L^2}, \tag{36}$$

which is equivalent [15] to the $H^1(\Gamma)$ inner product. In this sense, the matrix A^{-1} in (35) gives the "closest" vector η to the exact solution η_e in the space.

The orthogonal projection P onto $\ker(L)^\perp$ with respect to the basis $\{\varepsilon_i\}$ is given by

$$P = I_m - e\, e^T M. \tag{37}$$

The projection Q along $\ker(SL)$ onto $\text{range}(SL)$ in the basis $\{\varepsilon_i\}$ is given by

$$Q = I_m - e(e^T \widetilde{M} B e)^{-1} e^T \widetilde{M} B. \tag{38}$$

Note that Q annihilates any vector w which is constant on each Γ_j, i.e. any $w \in \text{colspan}(e)$, and leaves invariant any vector w for which $Bw \in \text{range}(L)$, i.e. for which $(e_k, Bw)_{L^2} = 0$ for $1 \le k \le d$.

4.4 Correcting B

As seen in Eq. (38), we require that the matrix $e^T \widetilde{M} B e$ be invertible. Since the columns of e are smooth functions on the grain boundary (being constant on each component Γ_j), we expect $e^T \widetilde{M} B e$ to be an accurate approximation of the matrix with components $(B_{\text{exact}} e_j, e_i)_{L^2(\Gamma)}$, which is invertible. It would be more satisfying, however, if the matrix $\widetilde{M} B$ were symmetric and negative definite. Moreover, it would be a disaster if one of the tiny eigenvalues $\mu_k = \lambda_k^{-1}$ of $K = Q\widetilde{E}^{-1}\widetilde{M} B Q$ turned out to be positive (or complex with positive real part), as the corresponding eigenmode in the expansion (19) would blow up almost immediately rather than decay rapidly to zero.

Without sacrificing accuracy, we want to alter B in order that the relation $(B\eta, \xi) = (B\xi, \eta)$ holds for all $\eta, \xi \in \text{span}\{\varepsilon_i\}$:

$$\xi^T \widetilde{M} B \eta = \eta^T \widetilde{M} B \xi, \qquad (\eta, \xi \in \text{span}\{\varepsilon_i\}). \tag{39}$$

We will correct B one subspace at a time, starting with functions η for which we can compute $B\eta$ most accurately, and proceeding until B satisfies (39) on all of $\text{span}\{\varepsilon_i\}$. To avoid confusion, let us denote the uncorrected version of B (obtained from X-Fosls) by $\widetilde{B}$.

The eigenfunctions u_k of the second derivative operator L form a nice basis for $L^2(\Gamma)$ because they are automatically orthogonal and become increasingly oscillatory as the eigenvalue increases. Let the matrix U diagonalize L with diagonal entries appearing in increasing order:

$$L = U D_L U^{-1}, \qquad (U^{-1} = U^T M). \tag{40}$$

This is easily done by diagonalizing the symmetric matrix $M^{-1/2} E M^{-1/2}$ to obtain D_L and $M^{1/2} U$ (which is unitary with respect to $\mathbb{R}^m$ instead of $L^2(\Gamma)$). The first d columns of U may be taken to be e from (34).

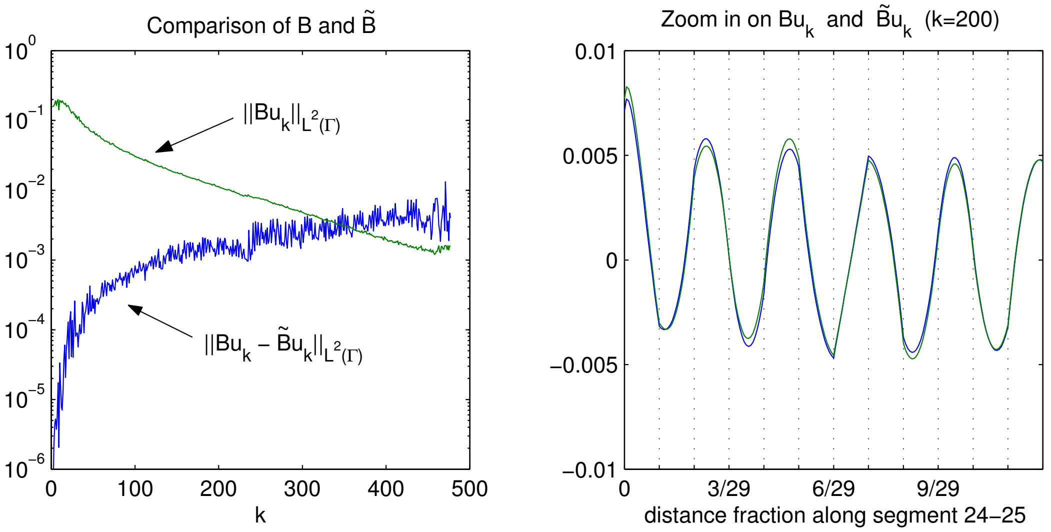

Fig. 11. Symmetrizing B alters Bu_k significantly only if u_k is highly oscillatory. Segment (24–25) of Fig. 6 has 29 line elements.

Next we form the matrix X representing $\widetilde{M}\widetilde{B}$ in the basis U:

$$X = U^T \widetilde{M}\widetilde{B}U. \tag{41}$$

We now seek the unit upper triangular matrix R such that XR is symmetric. All matrices X that we have encountered have the property that the pivots in the LU factorization are the diagonal entries, so we decompose $X = L_1 D_1 U_1$ and use $R = U_1^{-1} L_1^T$. We expect X to be nearly symmetric negative definite and $XR = L_1 D_1 L_1^T$ to be nearly identical to X. Figure 11 shows in what sense this is the case: the size of the correction made to Bu_k is extremely small relative to Bu_k unless u_k is highly oscillatory. But in that case, $\widetilde{B}u_k$ is not expected to be very accurate, so larger corrections are appropriate. As a result, most of the principal submatrices of R are very close to the identity. R itself turns out to be very well conditioned, so even the high frequency corrections are quite small; see Table 1.

There are several reasons for preferring a matrix of the form XR to some other symmetrized version of X such as $\frac{1}{2}(X + X^T)$ or $X_{\max(i,j),\min(i,j)}$. First, as the column index increases, the entries of X become less and less reliable as approximations to $(B_{\text{exact}} u_j, u_i)_{L^2(\Gamma)}$. As a result, we only wish to modify a given column using information which is at least as accurate as the column itself. This is why R should be upper triangular with ones along the diagonal. Second, the span of the first j columns of XR is the same as that of X. If the index j is small, the jth column of U is a smoothly varying continuous function on the grain boundary network. As a result, X-Fosls can compute Bu_j very accurately. But the solution Bu_j is *not* smooth due to discontinuities and infinite slopes at junctions. By restricting ourselves to corrections obtained by right multiplication, we leave the job of finding the appropriate asymptotic

Table 1
Condition numbers of R and Φ are small.

geometry	triangles	unknowns*	m	n	cond$(R)^\dagger$	cond$(M^{1/2}\Phi)^\ddagger$
Fig. 3	1264	15013	81	85	2.36	1.75
Fig. 3	5136	61317	161	165	2.33	1.83
Fig. 3	20588	246421	321	325	2.37	1.89
Fig. 16	6686	79920	477	506	2.76	2.08
Fig. 20	6788	81336	550	604	2.85	2.38

* degrees of freedom in grain boundary normal stress problem.

† R is used to symmetrize B. Φ diagonalizes K in Sec. 4.5.

‡ $\mathrm{cond}(M^{1/2}\Phi) = \|\Phi : \mathbb{R}^n_{l^2} \to \mathbb{R}^n_{L^2(\Gamma)}\| \, \|\Phi^{-1} : \mathbb{R}^n_{L^2(\Gamma)} \to \mathbb{R}^n_{l^2}\|$.

behavior of $g = B\eta$ at junctions to X-Fosls. In Figure 12, the projection $M^{-1}\widetilde{M}$ leads to larger oscillations on the right end because the angles at junction 25 in Fig. 6 deviate more from 120°, requiring a larger discontinuity in displacement jump. The fact that $(M^{-1}\widetilde{M}B)^{-1}u_1$ is a wild function shows that u_1 is not well suited for describing functions in range(B).

Replacing X by XR and $\widetilde{B}$ by B in Eq. (41), we obtain $M^{-1}\widetilde{M}B = UXRU^{-1}$. Note that $M^{-1}\widetilde{M}$ is the orthogonal projection in $L^2(\Gamma)$ from span$\{q_j\}$ onto span$\{\varepsilon_i\}$, and that B is only determined modulo ker$(\widetilde{M})$. We again leave the problem of determining the appropriate weights of singularities to X-Fosls, and require that range$(B) = $ range$(\widetilde{B})$. Let the columns of $Q_{\widetilde{B}}$ be a basis for

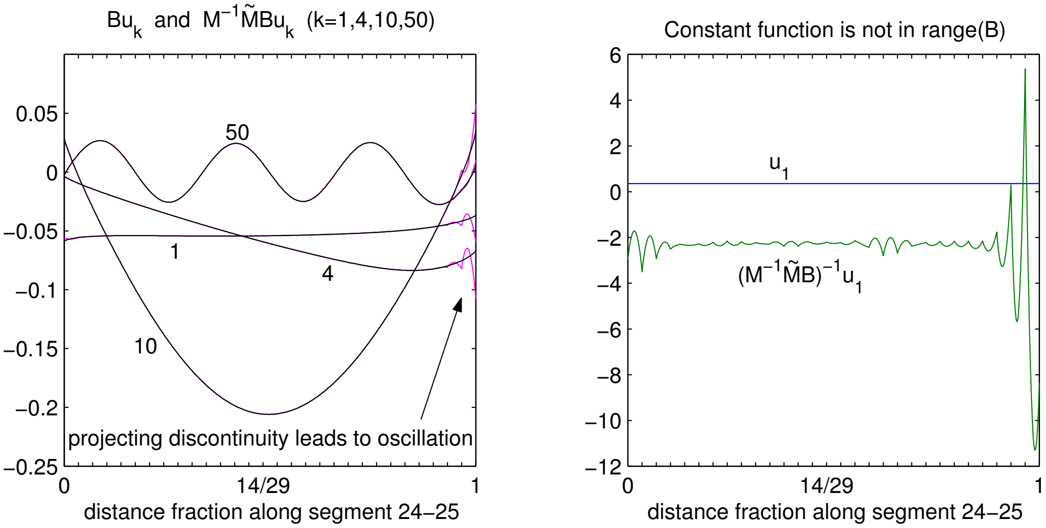

Fig. 12. Continuous functions are natural in the domain of B but not in the range, so it is best to alter B by right multiplication. (Geometry and junction labels: Fig. 6).

the kernel of $\widetilde{B}^T$ in $\mathbb{R}^n$. Then we define B via

$$\begin{pmatrix} M^{-1}\widetilde{M} \\ Q_{\widetilde{B}}^T \end{pmatrix} B = \begin{pmatrix} UXRU^{-1} \\ 0 \end{pmatrix}. \tag{42}$$

Since X is non-singular, $\mathrm{range}(\widetilde{B}) \cap \ker(\widetilde{M}) = 0$. Thus the rows of the matrix on the left are linearly independent, and the matrix is invertible.

4.5 Computing the eigenfunction expansion

The matrix representing K with respect to the basis $\{\varepsilon_i\}$ is obtained by matrix multiplication:

$$K = QA^{-1}BQ. \tag{43}$$

Note that K and Q are $m\times m$, A^{-1} is $m\times n$, and B is $n\times m$. Using (38), we find that the relation $\widetilde{M}BQ = Q^T\widetilde{M}B$ holds when $\widetilde{M}B$ is symmetric. Thus $K = (Q\widetilde{E}^{-1}Q^T)(\widetilde{M}B)$ is a product of two symmetric matrices, one positive semi-definite and the other negative definite. As a result, K is diagonalizable with real non-positive eigenvalues, and its kernel has dimension $d = \dim\ker(Q)$. We use dense linear algebra routines (from LAPACK) to solve the eigenproblem

$$K\Phi = \Phi D, \qquad D = \mathrm{diag}(\mu_1, \dots, \mu_m). \tag{44}$$

The first d columns of Φ may be taken to be e from Eq. 34, and we re-order the remaining columns so that

$$\mu_1 = \cdots = \mu_d = 0, \qquad \mu_{d+1} \le \cdots \le \mu_r < 0. \tag{45}$$

The columns ϕ_k of Φ are approximations of the eigenfunctions in the expansions (19). Next we wish to approximate the dual vectors ϕ_k^*. Applying B to both sides of $SL\phi_k = \lambda_k\phi_k$, we see that $LS(B\phi_k) = \lambda_k(B\phi_k)$. Thus $B\phi_k$ is an eigenfunction of the adjoint of SL with eigenvalue λ_k, and $\lambda_k \ne \lambda_j$ implies that ϕ_k is orthogonal to $B\phi_j$. The same holds for the numerical approximations: applying $\widetilde{M}B$ to $K\phi_k$ and arguing similarly, we conclude that ϕ_k is orthogonal to $\widetilde{M}B\phi_j$ in $\mathbb{R}^m$ if $\mu_k \ne \mu_j$. This means that up to roundoff error, $\Phi^T\widetilde{M}B\Phi$ will be block diagonal, with diagonal blocks of size b corresponding to eigenvalues of multiplicity b on the diagonal of D. Since $\widetilde{M}B$ is symmetric negative definite, we may compute the Cholesky decomposition

$$R^TR = -\Phi^T\widetilde{M}B\Phi, \qquad (R \text{ upper triangular}). \tag{46}$$

Next we re-define $\Phi = \Phi R^{-1}$ to achieve the condition $-\Phi^T\widetilde{M}B\Phi = I$. Because the right hand side of (46) is block diagonal up to roundoff error, this does not significantly intermix the eigenspaces. We define $\phi_j^* = -B\phi_j$ to obtain the set of dual vectors such that $(\phi_i, \phi_j^*) = \delta_{ij}$. We then set $a = \sqrt{\phi_j^T M \phi_j}$, $\phi_j = a^{-1}\phi_j$, $\phi_j^* = a\phi_j^*$ to achieve the normalization in Eq. (20). The λ_k are obtained via $\lambda_1 = \cdots = \lambda_d = 0$ and $\lambda_k = \mu_k^{-1}$ for $k > d$. Finally, the numerical operators SL and E_t are given by

$$SL\eta = \sum_{k=1}^{m} (\eta^T \widetilde{M} \phi_k^*) \lambda_k \phi_k, \qquad E_t \eta = \sum_{k=1}^{m} (\eta^T \widetilde{M} \phi_k^*) e^{\lambda_k t} \phi_k. \tag{47}$$

4.6 Efficiency considerations

The dense linear algebra being done here is quite inexpensive in comparison to the time it takes to set up and solve the stress problem to construct the matrix B. For the simple horizontal grain boundary geometry of Figure 3, we need to solve a sparse system of 15013 equations 81 times to obtain the 85×81 matrix B. After that, we are working with dense matrices with around 80 rows and columns, which can be diagonalized in less than a second on a 500 MHz single processor machine. For the more complicated geometries of Figures 16 and 20, we must solve systems with around 80000 equations approximately 500 times to construct B, and then do dense linear algebra on matrices with around 500 rows and columns. Because the stress problem is sparse, however, it scales significantly better with problem size than does the dense linear algebra, and for these problems the time spent computing X, R, Φ, D etc. is comparable to the time it takes to compute B (a few minutes). For a very long, narrow geometry, the ratio of grain boundary nodes to total nodes can be large enough that it takes longer to compute these matrices than it takes to set up B, but we have not encountered a situation where it was worth the effort to find alternatives to using standard dense linear algebra for this stage of the computation.

5 Results

In this section we apply the machinery developed in previous sections to study grain boundary diffusion for three different geometries. The first geometry consists of a rectangular interconnect line with a single horizontal grain boundary running through the center; see Fig. 3 of Sec. 3. The second geometry has a more complicated shape and a branching grain boundary structure; see Fig. 16. The third geometry also has a branching grain boundary structure, but with two connected components instead of one; see Fig. 20.

In Fig. 3, we show contour plots of some of the elasticity variables for the

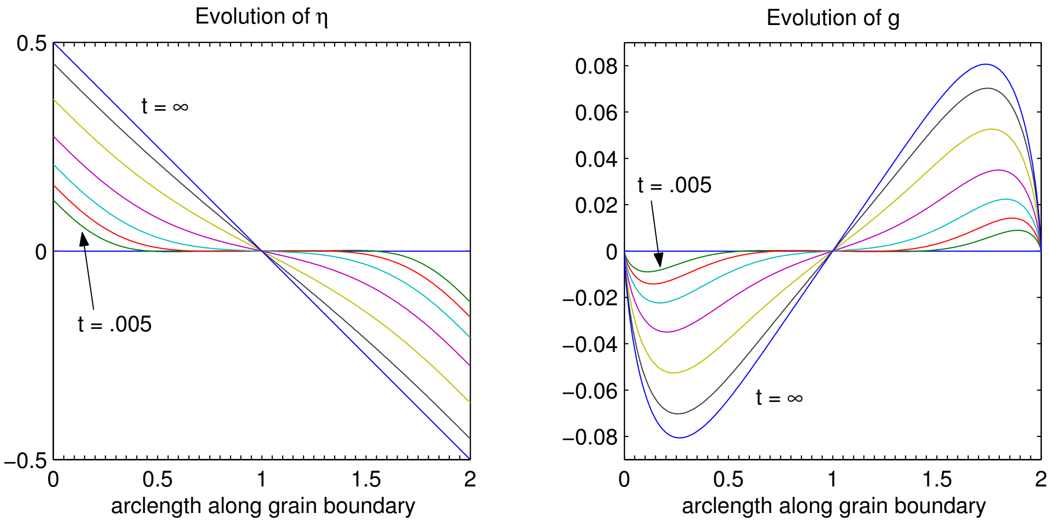

Fig. 13. Evolution of normal stress η and displacement jump g along the grain boundary for the geometry of Fig. 3 at $t = 0.005, 0.01, 0.02, 0.04, 0.08, 0.16, \infty$.

steady state stress distribution in which the gradient of the normal stress perfectly balances the electromigration force. The first two plots show the displacement variables u and v. Since atoms have migrated from left to right, the displacement jump $g = v^+ - v^-$ is negative on the left end of the grain boundary and positive on the right. The horizontal component of displacement u is non-zero due to the Poisson contraction effect: the right side of the line is under compression and the left side is under tension, so the material expands transversally on the right and contracts on the left, leading to a negative value of u throughout. Along the grain boundary, σ_{22} decreases linearly; but off the grain boundary, it behaves in a more complicated way, subject to the Lamé equations with Dirichlet boundary conditions at the walls. The shear force τ is strongest (in fact singular) near the ends because the Dirichlet boundary conditions on the walls must overcome the vertical wedging forces due to the loss or gain of material near the ends of the grain boundary.

In Fig. 13, we show the evolution of normal stress η and displacement jump g to steady state. The tick marks on the x-axis separate line elements on which η is quadratic and g is a linear combination of quadratic and self-similar functions. The evolution shown (and the displacement and stress fields of Fig. 3) were computed using the coarse mesh with 1264 triangles in Table 1. The normal stress is solved using Eq. (15) with $\eta_0 \equiv 0$

$$\eta(t) = E_t \psi - \psi, \qquad (t \geq 0) \tag{48}$$

and g is obtained from η by applying the operator B. E_t is computed via Eq. (47). We use a Poisson ratio for aluminum of 0.35 (so $\varkappa = 1.6$), and take $\psi_0 = 1$ on the right wall, deferring use of the correct dimensionless value of electric potential until (49) below. Using [3] $L = 10\mu\text{m}$, $\mu = 24.4$ GPa,

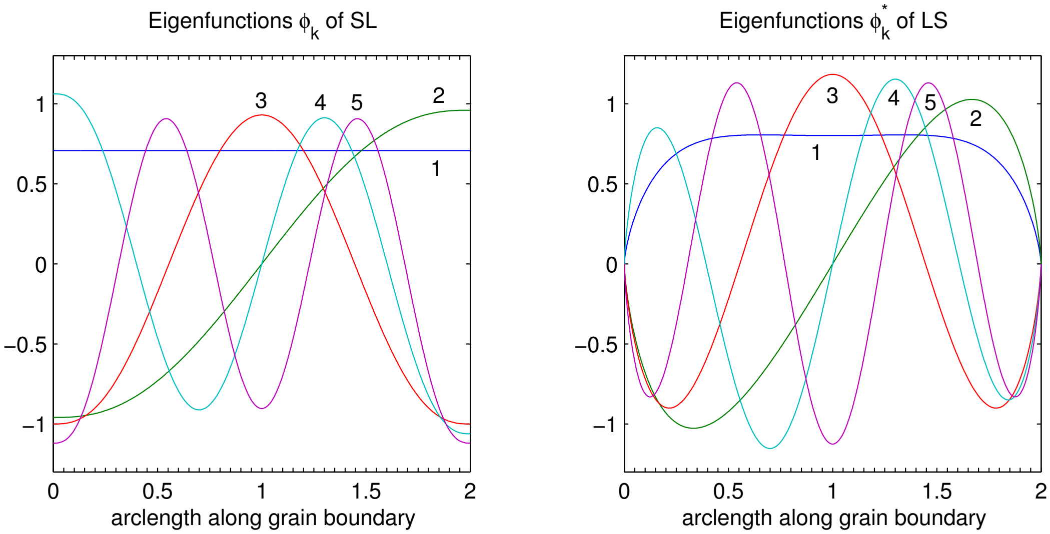

Fig. 14. The first five eigenfunctions ϕ_k of K (and SL) for the geometry shown in Fig. 3, along with the dual functions ϕ_k^* which satisfy $(\phi_i, \phi_j^*)_{L^2(\Gamma)} = \delta_{ij}$.

$\Omega_a = 1.68 \times 10^{-23}$ cm^3, $\nu_b = 1.5 \times 10^{15}$ cm^{-2}, $D_b = 10^{-8}$ cm^2/s, $T = 533$ K, and $k = 1.38 \times 10^{-23}$ J/K, we calculate the timescale $t_0 = \frac{kTL^3}{\nu_b D_b \Omega_a^2 \mu}$ to be 71000 s = 20 h. A more realistic geometry would be 10 times as long and 0.2 times as wide, which would increase t_0 by a factor of 1000 and decrease the dimensionless time at which steady state is achieved by a factor of about 50 due to the change in aspect ratio. To get physical values of stress, we multiply the dimensionless stress computed using $\psi_0 = 1$ by

$$\sigma^* = \mu\, \psi_0^{\text{correct dimensionless value}} = \frac{|Z^*|e}{\Omega_a} \psi_0^{\text{physical}}. \tag{49}$$

Taking the resistivity of aluminum to be 3.6μohm-cm and a current density of 20 mA/μm^2, we compute $\psi_0^{\text{physical}} = (.72 \text{ V/cm})(20\mu\text{m}) = 1.44$ mV. Using $Z^* = -5.0$ [3], we obtain the rough estimate $\sigma^* = 69$ MPa.

The qualitative behavior of the evolution is physically reasonable. The flux boundary conditions are immediately realized, causing the stress to have slope $-1/2$ at $x = 0$ and $x = 2$. Small depletion and accumulation regions appear near the ends shortly after the current is turned on. In between these regions, there is a steady flux caused by the electromigration force, but this does not lead to grain growth initially because atoms don't accumulate unless the flux is decreasing with position. These regions grow in size and move toward each other at a progressively slower rate, approaching the S-shaped steady state displacement jump which corresponds to a linearly decreasing normal stress which perfectly balances the electromigration force.

In Fig. 14, we plot the first several eigenfunctions ϕ_k of SL, along with the dual functions ϕ_k^*. Since $\phi_k \in \mathcal{D}(L)$, it satisfies zero flux boundary conditions; see

Eq. (6). Likewise, since $\phi_k^* \in \mathcal{D}(S)$, it satisfies $\phi_k^*(0) = \phi_k^*(2) = 0$; see Eq. (4a) of Fig. 2. For geometries with triple junctions, ϕ_k satisfies continuity and zero flux boundary conditions at each junction, while ϕ_k^* has discontinuities at each junction compatible with Eq. (5a) of Fig. 2. The corresponding eigenvalues are $\lambda_1 = 0$, $\lambda_2 = -12.5$, $\lambda_3 = -50.6$, $\lambda_4 = -126$, $\lambda_5 = -258$, which are the decay rates of the eigenmodes with respect to dimensionless time.

As mentioned in Sec. 3, when scaled appropriately, the eigenfunctions ϕ_k form a Riesz basis for $H^1(\Gamma)$. For convenience, we have instead chosen the $L^2(\Gamma)$ normalization

$$\|\phi_k\|_{L^2(\Gamma)} = 1, \qquad (\phi_i, \phi_j^*)_{L^2(\Gamma)} = \delta_{ij}. \tag{50}$$

This choice does not affect the fact that if $\eta \in H^1(\Gamma)$, then the expansions

$$\eta = \sum_{k=1}^{\infty} a_k \phi_k, \qquad E_t \eta = \sum_{k=1}^{\infty} a_k e^{\lambda_k t} \phi_k, \qquad a_k = (\eta, \phi_k^*)_{L^2(\Gamma)} \tag{51}$$

converge in $H^1(\Gamma)$. Although this covers the practical case of Eq. (48) since $\psi \in H^1(\Gamma)$ [15], it is natural to ask what happens if η belongs only to $L^2(\Gamma)$. The answer depends on whether $\{\phi_k\}_{k=1}^{\infty}$ with the normalization of (50) is a Riesz basis for $L^2(\Gamma)$, which happens if and only if the dual functions $\{\phi_k^*\}$ also form a Riesz basis [27]. Because the dual functions ϕ_k^* in Fig. 14 appear to be well scaled, and because the matrices Φ turn out to be extremely well conditioned (see Table 1 in Sec. 4.4), we conjecture that for $\eta \in L^2(\Gamma)$, the expansion $E_t \eta = \sum a_k e^{\lambda_k t} \phi_k$ converges in $L^2(\Gamma)$ for $t \geq 0$, and in $H^1(\Gamma)$ for $t > 0$. For the network version of the heat equation ($\eta_t = -L\eta$), this result is not difficult to prove; however, for grain boundary diffusion ($\eta_t = SL\eta$), a rigorous proof has not been found, and we must rely on numerical evidence.

In Fig. 15, we present a mesh refinement study for the geometry of Fig. 3. The coarsest mesh (used to produce Figures 3, 13 and 14) has 1264 triangles, 40 line elements on the grain boundary, and 81 grain boundary nodes. The finest has 20588 triangles, 160 line elements, and 321 grain boundary nodes. Eigenfunctions from the coarse and intermediate meshes are embedded in the fine mesh by interpolation without loss of information. Singular components of the dual functions from all three meshes are converted to piecewise quadratic functions on the fine mesh (by interpolation) to simplify the computation of norms in the lower left plot. Eigenvalues, eigenfunctions, and dual functions of index higher than 81 on the intermediate and fine meshes have been discarded in this figure. The order of convergence of $f(h)$ computed at $f_f = f(h)$, $f_i = f(2h)$ and $f_c = f(4h)$ is approximated by

$$\text{order of convergence} \;=\; (\log 2)^{-1} \log \frac{f_c - f_i}{f_i - f_f}. \tag{52}$$

The low order of convergence for the first few eigenfunctions is due to round-off error in the linear algebra and the fact that these eigenfunctions are

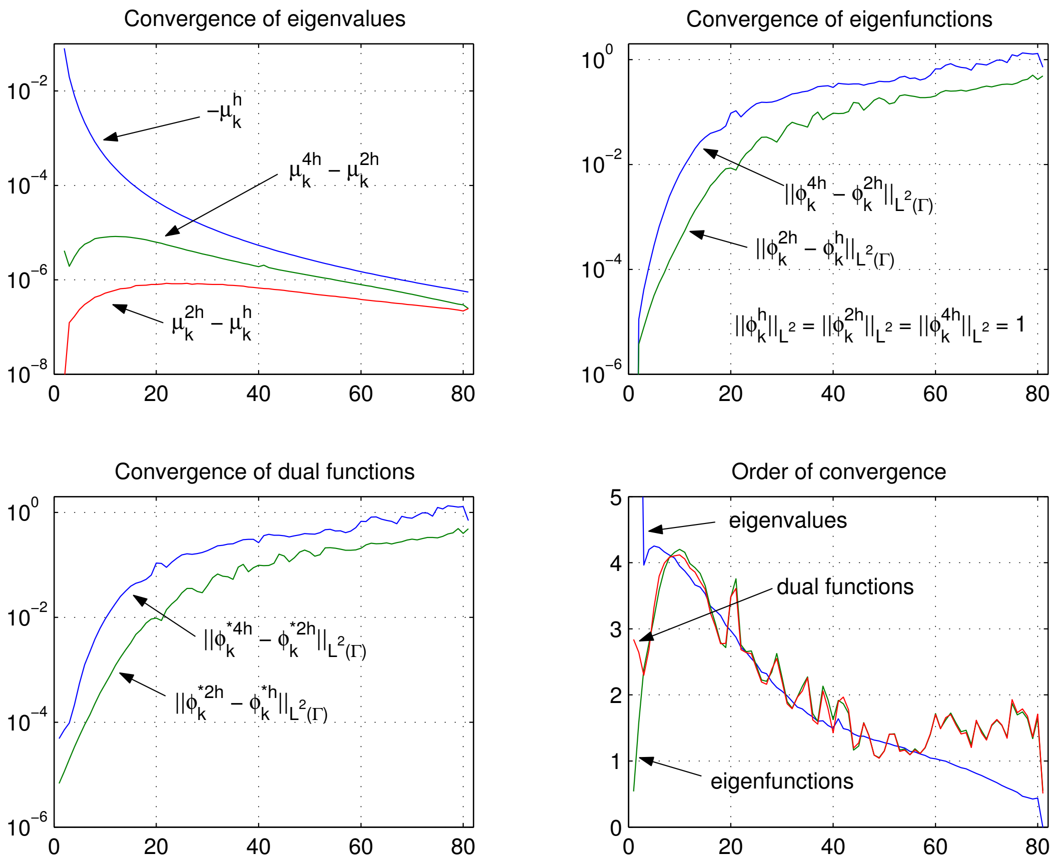

Fig. 15. Mesh refinement study for the geometry shown in Fig. 3. Note that the most important quantities, those of lowest index, are computed most accurately.

computed almost exactly on all three meshes. Third order accuracy is expected for smooth eigenfunctions since X-Fosls uses quadratic elements. Since $E_t\eta = \sum_{k=1}^{m}(\eta^T \widetilde{M}\phi_k^*)e^{\lambda_k t}\phi_k$ and $\lambda_k = \mu_k^{-1}$ becomes large and negative for large k, the most important μ_k, ϕ_k and ϕ_k^* are those of lowest index. We see from this figure that these are the quantities which are computed most accurately.

The second geometry we study is shown in Figures 16–19. The bounding box of the geometry is 4.25×2, and a mesh parameter $h = .035$ is used to obtain the triangulation shown in Fig. 5 (6686 triangles, 3797 vertices, 10476 edges). The grain boundary network has 238 line elements and 477 nodes. The normal stress problem leads to a sparse linear system with 79920 unknowns which must be solved 477 times to compute B. A total of 101 self-similar basis functions (Fig. 8) are used near corners and triple junctions to capture asymptotic behavior, several of them stabilized to avoid degeneracy; see [17].

In Fig. 16, the electrostatic potential ψ satisfies Laplace's equation with Dirichlet boundary conditions at the ends and Neumann boundary conditions on the side walls. We use quadratic C^0 (Galerkin) finite elements on the same mesh used for the grain boundary normal stress problem to compute ψ. Also shown

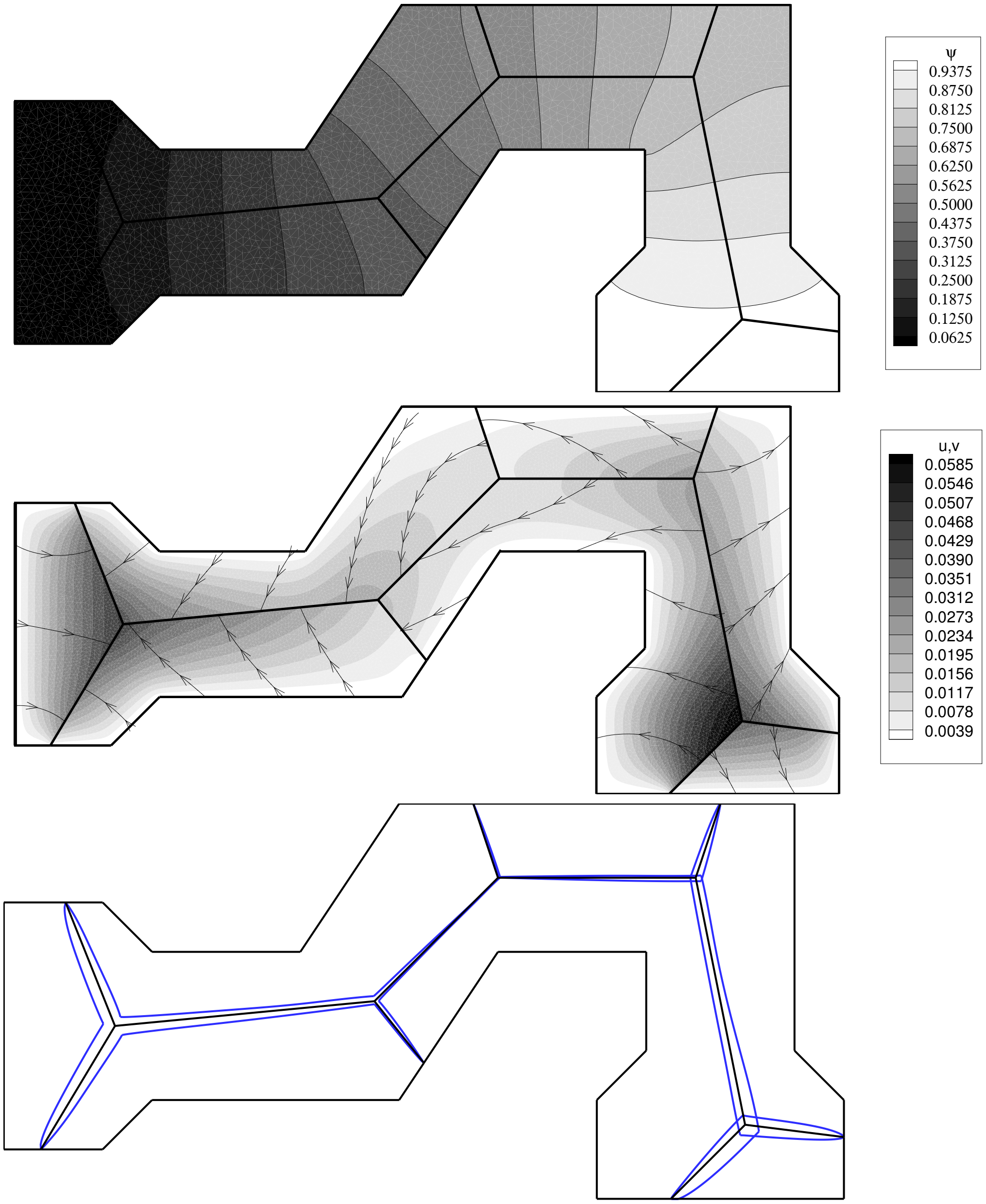

Fig. 16. Steady state electric potential, displacement, and displacement jump.

is a contour plot of the magnitude of the displacement field $\mathbf{u}$ in each grain (obtained via X-Fosls), together with streamlines tangent to $\mathbf{u}$. The bottom graph is an exaggerated view of the natural state of each grain obtained by plotting $x - C\mathbf{u}(x^+)$ and $x - C\mathbf{u}(x^-)$ as x ranges over Γ. Material has been transported from the left end of the interconnect line to the right; the grains must be zipped together ($g < 0$) on the left and pushed apart ($g > 0$) on the right in order to fit together in the stressed configuration.

In Fig. 17, we exhibit the steady state values of pressure, energy density and maximum shear stress. Note that the left and right ends of the line are gener-

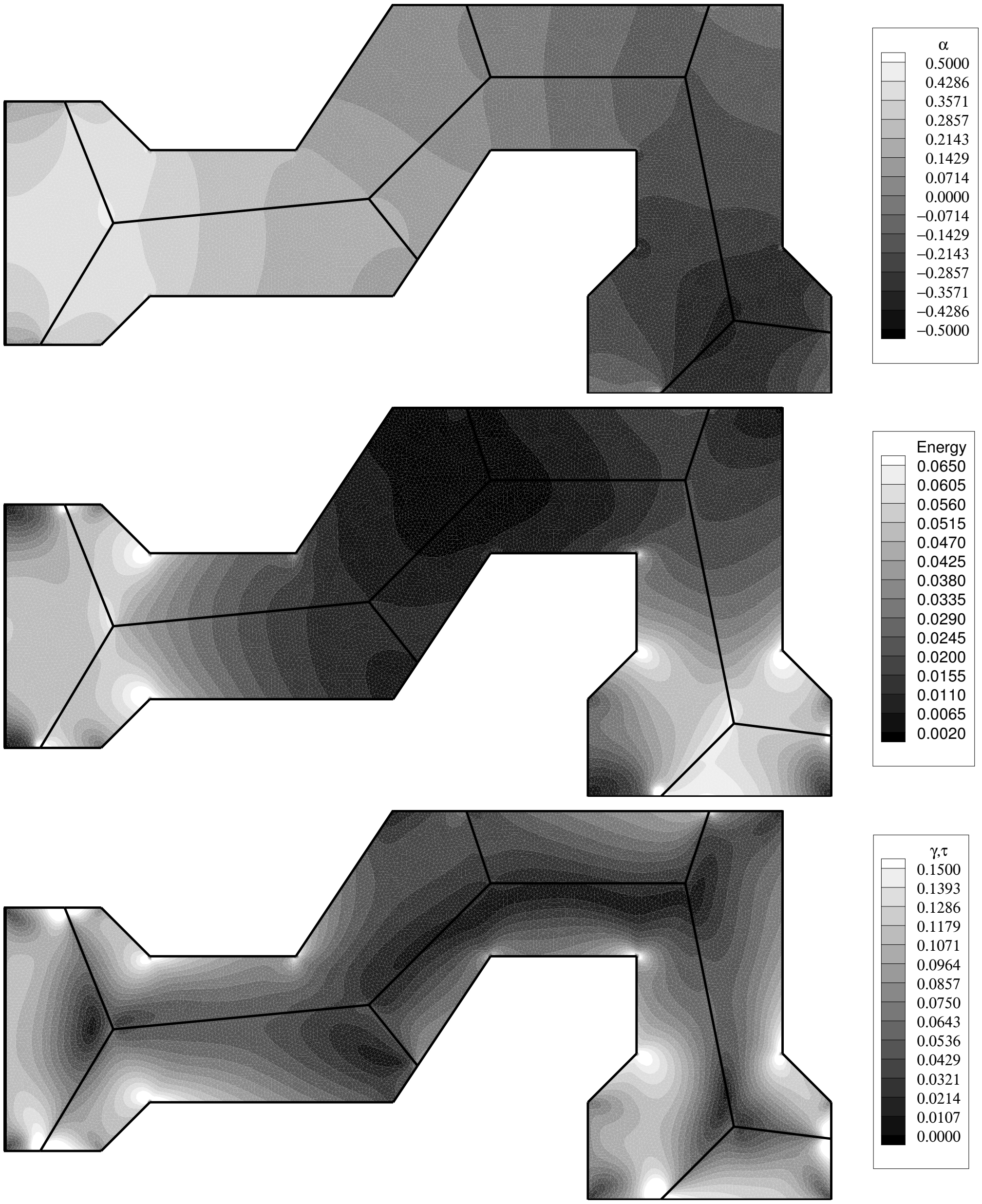

Fig. 17. Steady state distribution of (negative) pressure $\alpha = \frac{1}{2}(\sigma_{11} + \sigma_{22})$, energy density $E = \sigma_{ij}\epsilon_{ij} = \frac{\varkappa-1}{2}\alpha^2 + \gamma^2 + \tau^2$, and maximum shear stress $(\gamma^2 + \tau^2)^{\frac{1}{2}}$.

ally in a state of tension and compression, respectively, due to the transport of mass from left to right. We also observe that the stresses are largest where the grains have separated the most, and at re-entrant corners and grain boundary junctions where they have singularities.

In Fig. 18, we show the evolution to steady state of $\eta(x,t)$ and $g(x,t)$ along segment (25–7) of Fig. 6. The evolution of the full set of interwoven variables was shown in Fig. 10. Note that ψ does not vary linearly from left to right due to the complicated geometry, so the steady state normal stress $\eta = -Q\psi$ is not

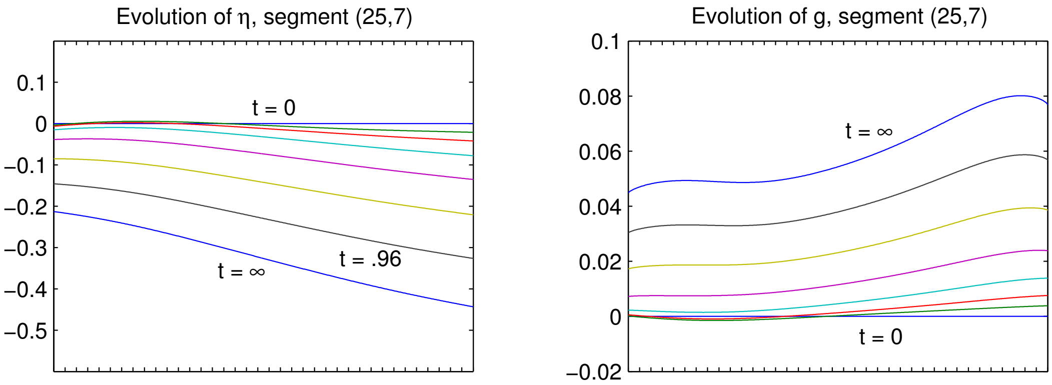

Fig. 18. Evolution of η and g at $t = .03, .06, .12, .24, .48, .96, \infty$.

as simple on each segment as it was for the rectangular geometry. The displacement jump g is discontinuous at the endpoints, i.e. g has a different limiting value at each junction when approached from a different segment. Moreover, g develops an infinite slope at the endpoints due to singularities. Asymptotically, $g \sim \sum c_i r^{\lambda_i}$, where r is the distance to the junction and $\lambda_i^{(7)} \in \{0, .799, .886\}$, $\lambda_i^{(25)} \in \{0, .725, .951\}$. The normal stress η remains well behaved even though a different linear combination $a = c_{ij}\sigma_{ij}$ of the stress components will generally diverge at the ends ($a \sim r^{\lambda-1}$, $\lambda^{(7)} \in \{.799, .886\}$, $\lambda^{(25)} \in \{.725, .951\}$). These exponents are known to double precision accuracy in the code.

In Fig. 19, we show the evolution to steady state of η and g along segment $(24, 27)$. Initially material leaves this segment, but the flux of mass at junction 24 changes sign near $t = .045$ and ultimately the grains accumulate material here. There are three things that contribute to this. First, the angle of the segment is such that $\psi(x)$ decreases as x moves from x_{24} to x_{27}; since the generation of stress generally acts to oppose the electromigration flux, we find that $\eta(x_{27}) > \eta(x_{24})$. Second, the segment lies to the right of the "center of mass" of the network, so eventually $\eta(x_{24})$ will be negative. And third, the segment is short, so it equilibrates more quickly than the structure as a whole. As a result, $\eta(x_{27}, t)$ increases relative to $\eta(x_{24}, t)$ on a shorter timescale than

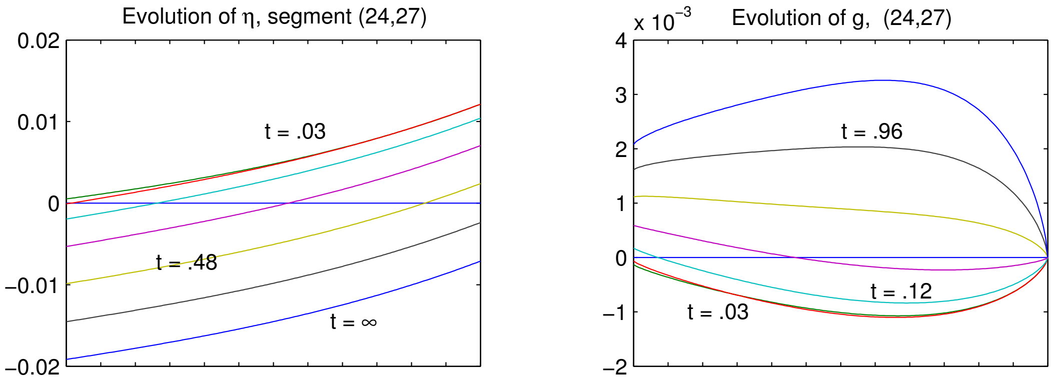

Fig. 19. Evolution of η and g at $t = .03, .06, .12, .24, .48, .96, \infty$.

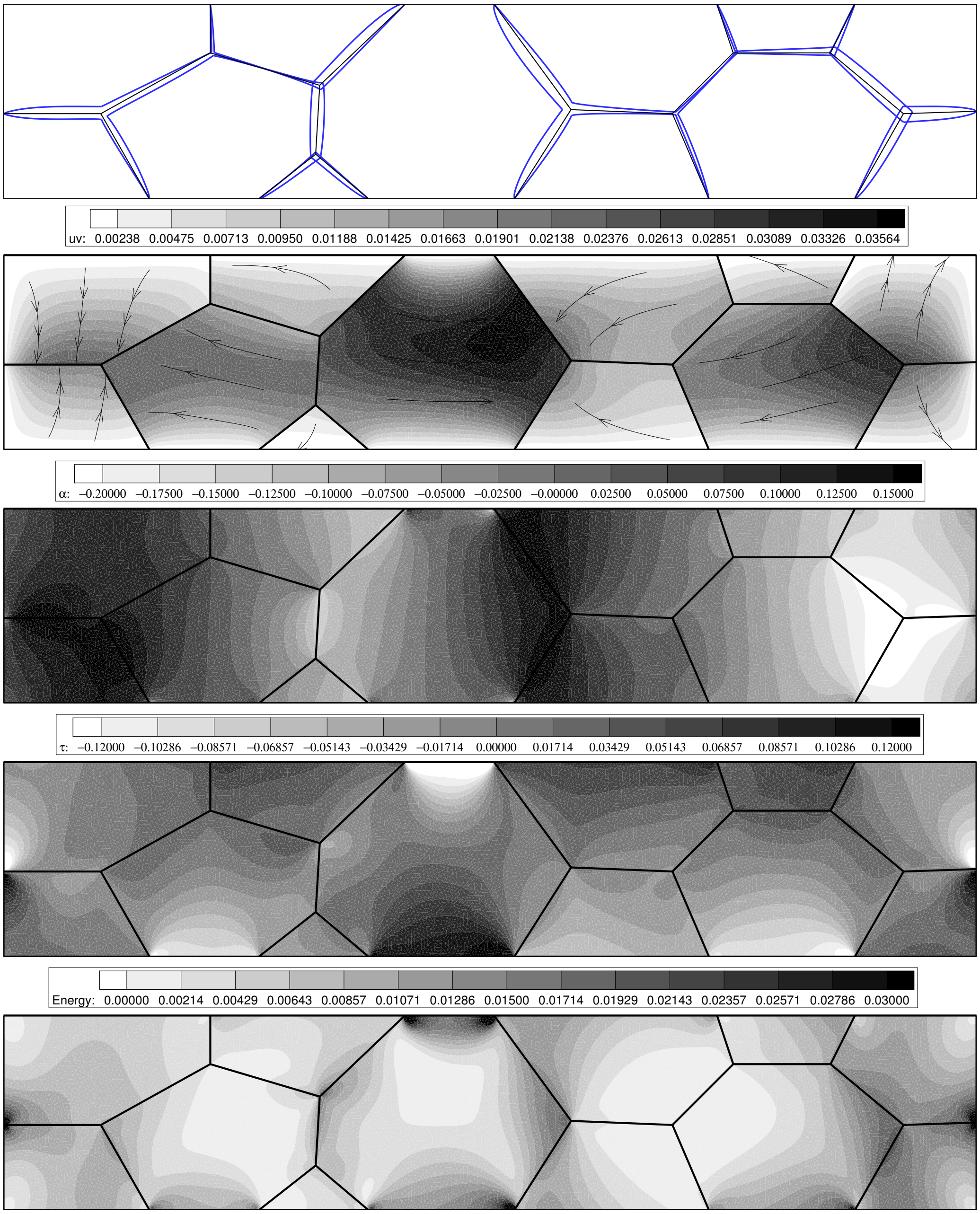

Fig. 20. Shapes of unstressed grains and contour plots of the steady state values of $\mathbf{u}$, α, τ, and E for a grain boundary network with two connected components.

the scale on which $\eta(x_{24}, t)$ settles into its eventual decreasing trajectory.

The third geometry we study in this section consists of a rectangular interconnect line with a grain boundary network with two connected components; see Fig. 20. The mesh used has 6788 triangles, 3856 vertices, 10632 edges and 550 grain boundary nodes, leading to a linear system with 81336 variables that is solved 550 times to compute B. A total of 80 self-similar basis functions were used near corners and triple junctions, stabilized when necessary.

On each component of Γ, material has been transported from left to right until the gradient of η balances the electromigration force. Large stress singularities develop at the gb–wall junctions where the grains are wedged apart (or pulled together) along grain boundaries and clamped in place by the walls. Note the large shear forces which develop near the top and bottom walls of the centermost grain to prevent it from sliding; it is being pushed from the left by grain growth and pulled from the right by grain annihilation.

The break in the network acts as a flux barrier to limit the effective length of the line by reducing the distance over which the stress gradient must balance the electromigration force. As a result, the maximum stress is smaller than it would be for a single component grain boundary network on an interconnect line of this length. The idea is similar to the observation that the maximum height of the function $y = x - 1/2$ on the unit interval is larger than the maximum height of the sawtooth $y(x < 1/2) = x - 1/4,\ y(x > 1/2) = x - 3/4$. In real materials, mass transport occurs at passivation interfaces as well, so material can be transported from one such structure to the next. This possibility would lead to larger stresses at the ends of the interconnect line and smaller stresses in the middle. It is interesting, however, that if passivation interfaces can be made with small enough diffusion coefficients, they can effectively inhibit the development of stresses in an interconnect line with disconnected grain boundaries.

6 Conclusion

We have presented an efficient numerical method for two-dimensional simulations of electromigration and stress driven grain boundary diffusion in polycrystalline interconnect lines. The method is based on new techniques from semigroup theory to represent the evolution and uses special basis functions to explicitly capture the singular asymptotic behavior of the stress tensor near grain boundary junctions to avoid loss of accuracy. The model does not include all physical phenomena that are important in mass transport in interconnect lines, but instead focuses on the role of stress.

Perhaps the most important insight to be gained from this work is the identification of a mechanism by which large “hidden” stress components may develop which are not directly involved in the diffusion process, but may play a role in void nucleation and stress induced damage. Put another way, the normal stress η (whose gradient on Γ contributes to the flux) remains finite for all time, behaving qualitatively as predicted by scalar “effective” stress models; however, the stress tensor still develops singularities at junctions — the singular components which combine to form η just happen to cancel. In real three dimensional interconnect structures with vias and faceted grains, it would be difficult to compute the asymptotic form of singularities a-priori as we have done in two dimensions. Moreover, such singularities would be mollified somewhat by plastic deformation and creep. Nevertheless, the general principle that stress components which are not directly coupled to the diffusion process may also cause damage seems useful, and could not be observed without modeling the full stress tensor.

A List of Variables

Table A.1
Important variables and operators

g	net grain growth $(g\mathbf{n} = \mathbf{u}^+ - \mathbf{u}^-)$
η	normal stress $(\eta = \mathbf{n} \cdot \sigma\mathbf{n})$
ψ	electric potential
σ	stress tensor $(\sigma_{11} = \mu[\alpha - \gamma], \quad \sigma_{12} = \sigma_{21} = \mu\tau, \quad \sigma_{22} = \mu[\alpha + \gamma])$
$\mathbf{u} = (u, v)^T$	displacement field
$\lambda, \mu, \varkappa$	elastic constants
$\Gamma, \Gamma_j, \Gamma_{J_k}$	grain boundary, grain boundary segment, connected component
$\{e_k\}_{k=1}^d$	basis for $\ker(L)^\perp$ (constant on connected components)
L	second deriv. operator on Γ $(A = L + I - P$ deals with kernel)
P	projection on $\ker(L)^\perp$
Q	non-orthogonal projection along $\ker(SL)$ onto $\mathrm{range}(SL)$
S, B	operators mapping $g \mapsto \eta$ and $\eta \mapsto g$ by solving elastic equations
E_t	semigroup governing η evolution
ϕ_k, ϕ_k^*	eigenfunctions and dual functions of SL
K	pseudo-inverse of SL (used to compute eigenfunctions)
λ_k, μ_k	eigenvalues of SL and K
λ	singularity exponent of a self-similar function
$\{q_j\}_1^n, \{\varepsilon_i\}_1^m$	finite element basis for g, η on Γ

References

[1] P. S. Ho, T. Kwok, Electromigration in metals, Rep. Prog. Phys. 52 (1989) 301–348.

[2] K.-N. Tu, J. W. Mayer, L. C. Feldman, Electronic Thin Film Science for Electrical Engineers and Materials Scientists, Macmillan, New York, 1992.

[3] W. W. Mullins, Mass transport at interfaces in single component systems, Metallurgical and Materials Transactions A 26A (8) (1995) 1917–1929.

[4] M. Schimschak, J. Krug, Electromigration-induced breakup of two-dimensional voids, Phys. Rev. Let. 80 (8) (1998) 1674–1677.

[5] Z. Li, H. Zhao, H. Gao, A numerical study of electro-migration voiding by evolving level set functions on a fixed cartesian grid, J. Comput. Phys. 152 (1999) 281–304.

[6] A. Averbuch, M. Israeli, I. Ravve, I. Yavneh, Computation for electro-migration in interconnects of micro-electronics devices, J. Comput. Phys. 167 (2001) 316–371.

[7] A. C. F. Cocks, S. P. A. Gill, A variational approach to two dimensional grain growth I. Theory, Acta Mater. 44 (12) (1996) 4765–4775.

[8] D. Moldovan, D. Wolf, S. R. Phillpot, A. Haslam, Mesoscopic simulations of two-dimensional grain growth with anisotropic grain-boundary properties, Phil. Mag. A 82 (7) (2002) 1271–1297.

[9] A. J. Haslam, D. Moldovan, S. R. Phillpot, D. Wolf, , H. Gleiter, Atomistic and mesoscale simulation of grain growth in nanocyrstalline thin films, Computational Materials Science 23 (2002) 15–32.

[10] M. C. Demirel, A. P. Kuprat, D. C. George, A. D. Rollett, Bridging simulations and experiments in microstructure evolution, Phys. Rev. Lett. 90 (1) (2003) 016106.

[11] R. Kirchheim, Stress and electromigration in Al-lines of integrated circuits, Acta metall. mater. 40 (2) (1992) 309–323.

[12] M. A. Korhonen, P. Borgesen, K. N. Tu, C.-Y. Li, Stress evolution due to electromigration in confined metal lines, J. Appl. Phys. 73 (8) (1993) 3790–3799.

[13] A. F. Bower, D. Craft, Analysis of failure mechanisms in the interconnect lines of microelectronic circuits, Fatigue Fract. Eng. Mater. Struct. 21 (1998) 611–630.

[14] D. Fridline, Finite element modeling of electromigration and stress voiding in microelectronic interconnects, Ph.D. thesis, Brown University (2001).

[15] J. Wilkening, L. Borucki, J. A. Sethian, Analysis of stress driven grain boundary diffusion, SIAM J. Appl. Math (submitted).

[16] J. Wilkening, Mathematical analysis and numerical simulation of electromigration, Ph.D. thesis, University of California, Berkeley (May 2002).

[17] J. Wilkening, Extended first order system least squares finite elements for plane elasticity, J. Comput. Phys. (in preparation).

[18] M. Berndt, Adaptive refinement and the treatment of discontinuous coefficients for multilevel first-order system least squares (FOSLS), Ph.D. thesis, University of Colorado at Boulder (1999).

[19] Z. Cai, T. A. Manteuffel, S. F. McCormick, First-order system least squares for second-order partial differential equations: Part II, SIAM J. Numer. Anal. 34 (2) (1997) 425–454.

[20] Z. Cai, T. A. Manteuffel, S. F. McCormick, First-order system least squares for the Stokes equations, with application to linear elasticity, SIAM J. Numer. Anal. 34 (5) (1997) 1727–1741.

[21] C. Daux, N. Moes, J. Dolbow, N. Sukumar, T. Belytschko, Arbitrary branched and intersecting cracks with the extended finite element method, International Journal for Numerical Methods in Engineering 48 (2000) 1741–1760.

[22] L. D. Landau, E. M. Lifshitz, Theory of Elasticity, 3rd Edition, Butterworth–Heinemann, Oxford, 1986.

[23] P. G. Ciarlet, Mathematical Elasticity, Vol. 1, North–Holland, Amsterdam, 1993.

[24] I. A. Blech, C. Herring, Stress generation by electromigration, Applied Physics Letters 29 (3) (1976) 131–133.

[25] E. Hille, R. S. Phillips, Functional Analysis and Semi-groups, American Mathematical Society, Providence, 1957.

[26] K. Yosida, Functional Analysis, Springer-Verlag, Heidelberg, 1980.

[27] I. C. Gohberg, M. G. Krein, Introduction to the Theory of Linear Nonselfadjoint Operators, Vol. 18 of Translations of Mathematical Monographs, American Mathematical Society, Providence, RI, 1969.

[28] B. A. Plamenevskij, Elliptic boundary value problems in domains with piecewise smooth boundary, in: M. S. Agranovich, Y. V. Egorov, M. A. Shubin (Eds.), Partial Diff. Eqs. IX, Vol. 79 of Encycl. Math. Sciences, Springer, Berlin, 1997.

[29] P. Grisvard, Singularities in Boundary Value Problems, Vol. 22 of Research Notes in Applied Mathematics, Masson, Paris, 1992.

[30] M. Costabel, M. Dauge, Y. Lafranche, Fast semi-analytic computation of elastic edge singularities, Computer Methods Appl. Mech. Engr. 190 (2001) 2111–2134.

[31] S. I. Larimore, An approximate minimum degree column ordering algorithm (COLAMD/SYMAMD), Master's thesis, University of Florida (1998).

[32] L. P. Franca, T. J. Hughes, Two classes of mixed finite element methods, Computer Methods in Applied Mechanics and Engineering 69 (1988) 89–129.

[33] D. Braess, Finite Elements – Theory, fast solvers, and applications in solid mechanics, Cambridge University Press, Cambridge, 1997.